Title
A First Principles Study of Mass Transport in the Dehydrogenation of Lithium Amides and Lithium Alanates

Author
Rolih, Biljana

Publication Date
2014

Peer reviewed|Thesis/dissertation

University of California

Los Angeles

A First Principles Study of Mass Transport in the Dehydrogenation of Lithium Amides and Lithium Alanates

A dissertation submitted in partial satisfaction

of the requirements for the degree

Doctor of Philosophy in Chemistry

by

Biljana Rolih

2014

Abstract of the Dissertation

A First Principles Study of Mass Transport in the Dehydrogenation of Lithium Amides and Lithium Alanates

by

Biljana Rolih

Doctor of Philosophy in Chemistry

University of California, Los Angeles, 2014

Professor Vidvuds Ozolins, Chair

The pursuit of competitive alternatives to energy derived from the combustion of fossil fuels, has led to a great variety of new technologies. Exceptional developments in electrochemical storage and production promise to lead to clean burning passenger vehicles. The high chemical density of a hydrogen fuel cell enables it to meet current standards for driving range and weight required of vehicles, making it an excellent candidate for universal application in the automotive industry. One of the biggest obstacles the fuel cell industry has yet to overcome is the means of practical hydrogen storage. Solid state metal hydrides are a class of materials that show potential for both economic and practical hydrogen storage. The search for the ideal metal hydride is defined by thermodynamic and kinetic constraints, since the requirements for a viable system are a rapid release of hydrogen in the temperature range of -40°C, to 80°C.

First-principles density functional theory is an excellent method for gaining insight into the kinetics and thermodynamics of metal hydride solid state reactions. In

the work presented here, density functional theory is used to explore formation energies, concentrations and migration barriers of metal hydrides. In particular, the following systems were analyzed:

- Li - N - H It is well known that the reactive hydride composite $LiNH_2$ + LiH reversibly releases a large amount of hydrogen gas, with more favorable thermodynamics than $LiNH_2$ alone. Kinetics of mass transport during the dehydrogenation of $LiNH_2$ + LiH are investigated. A model is developed for determining activation energies of native defects in bulk crystals. In order to establish whether mass transport is the rate-limiting step in the dehydrogenation reaction, results are compared to experimental values.

- Li - Al - H Kinetics of mass transport during the dehydrogenation of the metal hydride $LiAlH_2$ are investigated. It is known that $LiAlH_4$ endothermically decomposes via a two step reaction. The kinetics of both steps in the reactions are studied. Results are compared to experiments in order to determine whether mass transport is the rate-limiting process in the reactions.

The dissertation of Biljana Rolih is approved.

Anastassia Alexandrova

Alex Levine

Vidvuds Ozolins, Committee Chair

University of California, Los Angeles

2014

to my family

Table of Contents

List of Figures

List of Tables

Acknowledgments

Firstly, none of this work would have ever been possible without the support and mentorship of my adviser Professor Vidvuds Ozolins. I am infinitely grateful for the endless hours he spent going over my work with me, and answering my questions. He taught me not only a great deal about the science of my work, but also how to think more critically. Most importantly he showed me how to persist and stay curious in the face of colossal frustration.

I extend my utmost gratitude to members of my group who have been tremendously helpful in advancing my knowledge. Special thanks to Dr. Kyle Michel, and Dr. Hakan Gunaydin for extensive beginner training in the finesse of computational modeling. Dr. Fei Zhou for patiently answering every question under the sun. Other members of my group who have been a joy to work with: Weston Nielson, Chi-Ping Liu, Chao Yu, Yi Xia, Hao Lin, Yongduo Liu, Eric Dhall, Pattanasak Teeratchanan.

I would also like to thank the members of my dissertation committee, Professor Alex Levine, Professor Anastassia Alexandrova and Professor Miguel Garcia-Garibay for their guidance on my research and my future. Special thanks to Professor Alex Levine, Professor William Gelbart, and Professor Ben Schwartz for the valuable and enjoyable graduate physics courses.

Additionally I would like to thank my friends and family for their love and support. Endless gratitude to my sister Jelena, my mother Nada and my father Leopold, because their support has enabled me to accomplish more than I ever thought possible. Thank you for inspiring me and teaching me to love good work. All of my friends for their faith and understanding, most notably, Dr. Katerina Podshivalova, Dr. Erin Greiner, Dr. Elinne Becket, Dr. Fernando Uribe-Romo,

Dr. Rachel Harper, Dr. Yuen Lau, Masha Rotfeld, Dayanara Parra and Sofiya Zhovnovataya.

Financial support for the research has been provided by the US Department of Energy, Office of Energy Efficiency and Renewable Energy under Contract No. DE-FC36-08GO18136, titled "Efficient Discovery of Novel Multicomponent Mixtures for Hydrogen Storage: A Combined Computational/Experimental Approach". Additionally it has also been funded by the US Department of Energy, Office of Science, Basic Energy Sciences under Grant. No. DE-FG02-07ER46433, titled "Quantum Prediction of Advanced Hydrogen Storage Materials".

Vita

2006	B.S. (Physics) University of California, Santa Barbara.
2007 – 2010	Teaching Assistant, Department of Chemistry, Taught sections in Introduction to Chemistry, Introduction to Chemistry Laboratory Techniques, and Statistical Mechanics for graduate students.
2008 – 2009	Graduate Researcher for Professor Alex Levine.
2010 – 2014	Graduate Researcher for Professor Vidvuds Ozolins

Publications

Rolih, B. and Ozolins, V. (March,2013)*Bulk Diffusion via a Kick-Out method for Lithium in the Decomposition Reaction LiAlH4/Li3AlH6* Paper presented at the March meeting of the American Physical Society, Baltimore, MD

Rolih, B. and Ozolins, V. (November,2012)*Mass Transport for the Decomposition Reactions LiNH2/LiH and LiAlH4/Li3AlH6* Paper presented at the November meeting of the Materials Research Society, Boston, MA

Rolih, B. and Ozolins, V. (March, 2012) *Bulk Diffusion of Defects in LiAlH4/Li3AlH6* Paper presented at the March meeting of the American Physical Society, Boston, MA

Rolih, B. and Ozolins, V. (March, 2011) *Kinetics of Mass Transport of Native Defects in $LiNH_2$ + LiH* Paper presented at the March meeting of the American Physical Society, Dallas, TX

CHAPTER 1

Introduction to Hydrogen Storage and PEM Fuel Cells

1.1 Introduction

Economic and technological progress have historically been linked to the capability of generating cheap and abundant energy. With rising population growth, it's not surprising that energy demand is increasing at a rate of 1-2%, both in the U.S. and world markets [1]. The majority of industries depend primarily on energy from fossil fuels, which are arguably both indispensable and controversial. The first issue is the matter of availability. Since the nineteenth century there have been several alarming predictions of the depletion of recoverable crude oil supply. However thanks to innovative new technologies in oil refining, recoverable crude oil sources have never reached the point of exhaustion. Additionally new frontiers of on and off shore oil supply still remain to be explored. For instance, in recent years, U.S. production from tight oil and shale formations has seen a near fourfold increase between 2008 and 2013 [2]. While the size of the total crude oil reservoir remains debatable, the current estimate is 3,357 billions of barrels [3]. In just a few years of innovation for natural gas recovery, the increase in total recoverable resources due to inclusion of shale oil and shale gas, rose by 11% of the total estimated crude oil supply [3, 4]. Though the exact quantity of recoverable shale

oil is subject to change as more information becomes available from geological surveys, it's evident that shale oil is a substantial part of the global crude oil supply. In spite of recent progress in the energy industry, public concern that we are running out of oil persists, though even the most conservative projections suggest stable natural gas, and crude oil supply, and production for the following decades [2]. It is however implausible that the actual, so far unproven supply of fossil fuels is unlimited, and a future with a variety of alternate energy sources is inevitable.

The more cumbersome issue with fossil fuels stems from environmental concerns, primarily due to excessive release of greenhouse gases into the atmosphere from the combustion of fossil fuels [5]. The global goal is to phase out energy dependence on fossil fuels over several decades. However, transitioning to alternative energy sources is a challenge. Some of the alternative methods of generating power are wind, solar or nuclear power sources. Wind generation, and solar have already been established as large scale power sources. Moreover their practicality is limited. While sunlight is abundant in many areas, like the southwest of the U.S., it is generally intermittent, since overcast days are difficult to predict. For wind power generation intermittence is an even bigger problem. Storing solar energy is also problematic. While there are solar drip feed batteries available for energy storage, they are large and expensive, and generally better suited for small scale distribution, like in private homes, than a large scale power grid. In order for a system to be seriously considered as a replacement for fossil fuels, means of storing surplus power from alternative sources, such as wind and solar must be developed.

The current forms of alternative energy storage are not universally applicable. Instead each approach has distinct advantages in particular niche markets. For instance, some examples of energy storage are electrochemical (batteries) and

electrical (capacitors and super capacitors) which have applications in providing energy on small scale and in mobile devices, whereas wind power is better suited for providing power to cities. Mobile applications in particular are becoming increasingly more demanding in international markets. Currently the most popular method of energy storage in mobile devices is batteries. However with rising popularity of mobile and handheld devices, other options for small scale storage are likely to soon be integrated.

The Ragone plot in Fig.1.1 reveals the benefits and downsides of the electrochemical systems. The Fuel cell can be considered high-energy systems, and the capacitor a high-power system. The high energy densities of hydrogen storage systems makes them a more ideal candidate for integration in cars. Though energy cannot be drawn as fast as in capacitors due to low power density, but in vehicles where a finite amount of energy can be stored, and which relies on only infrequent recharging, a high energy density is a more substantial eligibility criteria. However fossil fuels, and the gas turbine are easily still the best available option today, as can be seen on the plot they are both high-energy and high-power. Furthermore fuel cells are still not competitive with fossil fuels due to high cost of production and inadequate durability and lifetime. More research should be dedicated to develop this potentially excellent energy generation system and make it competitive in the automotive industry.

1.2 Summary on PEM Fuel Cells

The general idea of how fuel cells work is using the energy from a chemical reaction by converting it to electrical energy via a proton exchange membrane. The improvement upon the traditional ICE engine, is that the external electrical circuit

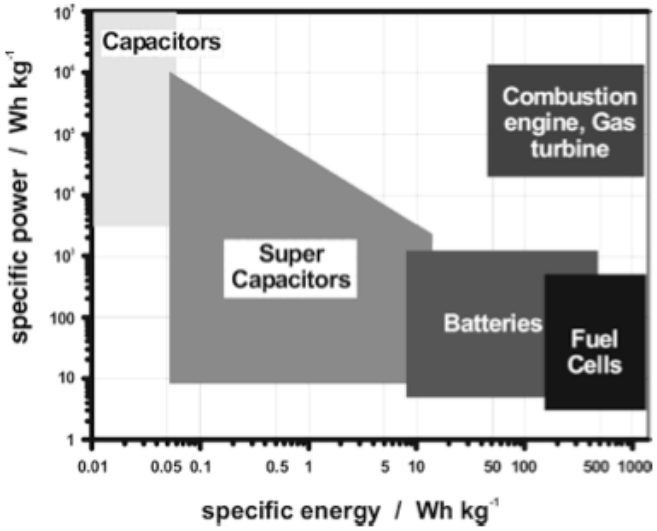

Figure 1.1: Ragone plot showing relations for energy systems [6].

on a fuel cell works at 40-60% efficiency. In the future, researchers are hoping to push that number up to 70% [6].

Factors that contribute to the discrepancy in practical and theoretical efficiency in fuel cells are three fold. Firstly, there are inactive components to the system, such as current collectors, containers, or conductive dilutants. Secondly, internal losses due to resistance between the electrolyte and electrode, and other parts of the cell. Lastly, the limited use of active masses in a fuel cell, such as passivation of electrodes, which can leave them electrochemically inert. Still these factors are minute, and the efficiencies in fuel cells are far superior to the internal combustion engine with a theoretical efficiency of 37% (and practical 18-20%), due to the limitations of the Otto cycle [7].

The basic design of a fuel cells consists of two current collecting bipolar plates enclosing the core structure, known as the membrane electrode assembly (MEA). This set up can be seen in Figure 1.2. The gas diffusion chamber (GDC) forms the outer layer of the MEA and is in contact with the bipolar plate where gaseous

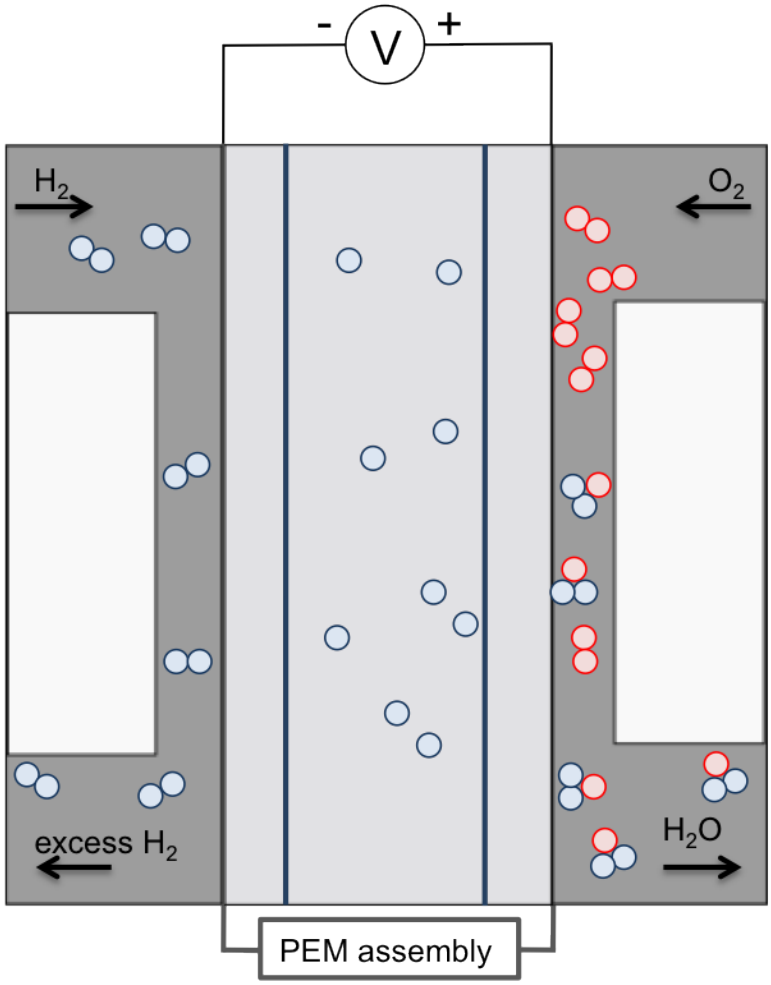

Figure 1.2: Schematic of a PEM fuel cell.

hydrogen is channeled into the anode, and oxygen from the air into the cathode. Each gas diffusion chamber is coated with a thin catalyst layer and separated by the PEM. Together the gas diffusion chamber and the catalyst layer make up what is considered the electrode. To assemble the complete fuel cell, the flow-field plates and the MEA, the components are manufactured individually, then pressed together at high temperatures and pressures [8].

Electrons are separated at the anode, and conducted to the external circuit.

Within the catalyst layer, the hydrogen dissociates into electrons and hydrogen ions. The redox reaction at the anode is denoted by:

$$2H_2 \rightarrow 4e^- + 4H^+. \tag{1.1}$$

where the electrons are rerouted to an external circuit and the hydrogen ions are passed on through the PEM to the cathode. The redox reaction at the Cathode is given by

$$4e^- + 4H^+ + O_2 \rightarrow 2H_2O. \tag{1.2}$$

where the hydrogen combines with oxygen from the air to form water. The excess energy is converted into electrical current.

The Hydrogen is stored directly bordering cathode side and pumped into the gas channel. To date, a variety of methods of storing the hydrogen supply are used: gaseous storage of compressed hydrogen, liquid storage of cooled, compressed gas and solid state storage. Compressed liquid and gaseous hydrogen storage systems are both excellent reversible storage options, however they do have some drawbacks. Due to high pressures (350 bar and 700 bar) the system requires a robust tank, capable of meeting the stress, strain and safety standards for a high pressure gas tank [9, 10]. In order to meet all requirements, tanks are reinforced with carbon fibers, which are responsible for over 65% of the total cost. Another key challenge with compressed hydrogen is increasing the volumetric capacity limit. One known method involves compressed cryogenic hydrogen. At low temperatures, the density of elemental hydrogen decreases as temperatures continue to

decrease. Therefore, to improve the volumetric capacity, hydrogen is compressed and cooled from room temperature to liquid nitrogen temperature (77 K). This method improves the volumetric capacity by a factor of three. [9] Ultimately, implementing gaseous hydrogen comes down to optimizing weight, volume and cost. Liquid hydrogen stores more elemental hydrogen than compressed, cooled gaseous H_2, 0.070 kg/L vs. 0.039 kg/L at 700 bar. However it is not without its own set of challenges. Storing liquid hydrogen close to room temperature, required for on board storage, results in hydrogen loss due to boil-off. While a system with a liquid hydrogen supply enjoys an extended driving range [9], the cost of the tank is still too high, making hydrogen cars not competitive in the automobile industry. Solid state storage depends either on chemisorption or physisorption. Chemisorption is a process wherein chemical bonds are alternately created and broken, depending on easily manipulated thermodynamic parameters. Physisorption is a process wherein molecules under pressure enter a porous material, but do not form chemical bonds to the host. Examples of hydrogen storage materials by physisorption are metal organic frameworks [11]. While they can store an acceptable percentage of gas [12, 13] their disadvantage lies in the operating temperatures of about 77K, which are too low for practical applications. In this work we will focus on solid storage of hydrogen via chemisorption, or the breaking and creating of chemical bonds.

In order to narrow down the search for viable materials the DOE has determined a set of physical requirements that must be met by the material. The goal for the gravimetric capacity, or the usable specific-energy from hydrogen is set at 2.7 kWh/kg, 7.5 w% H_2 and the volumetric capacity, or the usable energy density from H_2 as 1.5 kWh/L. [9, 14]. Thermodynamic and kinetic constraints on the desired material determine the temperature range that controls hydrogen release

and uptake, and the speed of these reactions. Target temperatures for the hydrogen release reaction is between -40 to 80 C and pressure range of 3 to 12 bar, why hydrogen uptake should occur at ambient temperatures. The speed of these reactions must be no less than 2.0 kg H_2/min. [6] Enthalpy change in solid state reactions is primarily determined by hydrogen. A metal hydride should have an enthalpy of formation change between 20 to 40 kJ/mol H_2.

1.3 Solid State Metal Hydrides

A viable class of materials that meets the requirements for hydrogen storage are metal hydrides. Metal hydrides and alloys are capable of reversibly storing hydrogen by incorporating atomic hydrogen into their lattice structure. Metal hydride refers to a class of materials consisting of a metal binding to atomic hydrogen. Metal hydrides can be further broken down into binary (M_aH_b), and more complex structures, such as ternary metal hydrides ($M_aX_bH_c$) [15].

The manufacturing process of metal hydrides involves heating the metal under gaseous hydrogen pressure. Before hydrogen is absorbed into the bulk, first molecular hydrogen dissociates while adsorbed at the surface. Hydrogen exothermically forms a high energy chemical bond once it dissolves in the bulk metal [16]. Furthermore the hydrogen is located on either tetrahedral or octahedral sites of the metal lattice.

Binary metal hydrides are classified by the type of chemical bond that the metal shares with the hydrogen. Due to its unique nature of exhibiting a variety of oxidation states, hydrogen can act as either the cation or the proton in the bond, therefore generally the electronegativity of the metal determines the type of bonding [17]. It has also been reported that there is a linear correlation between

Table 1.1: Examples of dehydrogenation enthalpies for simple metal hydrides

Reaction	$\Delta H^{formation}$ (kJ/mol)
($LiH \rightarrow Li + \frac{1}{2} H_2$)	181.0 [19]
($NaH \rightarrow Na + \frac{1}{2} H_2$)	112.6 [19]
($MgH_2 \rightarrow Mg + H_2$)	75.2 [19]
($KH \rightarrow K + \frac{1}{2} H_2$)	115.3 [19]
($CaH_2 \rightarrow Ca + H_2$)	183.6 [19]

the electronegativity of the cation and the thermal desorption temperature, T_d, for a series of metal-borohydrides [18]. It has been suggested that electronegativity of the metal cation might be a good criterion for estimating T_d and aiding in the search for new favorable reactions.

Examples of simple metal hydrides and the desorption enthalpies are presented in Table 1.1. Cations heavier than calcium are not considered, as they would make the application system impractical, and while hydrides with other cations lighter than Ca exist they are disregarded for either being toxic, or too stable. From this we glean that simple metal hydrides are not viable for storage purposes, as their enthalpies of desorption are too high.

The assumption is that fine tuning of several criteria of the materials will lead to an eventual candidate for hydrogen storage. In order to satisfy the criteria for high gravimetric and volumetric density, only the lighter metals are considered. Lighter metals are crucial, especially in the case of ternary hydrides, which are the best candidates according to thermodynamics. Thus the search for a hydrogen storage material is limited to a small number of possible components. Ternary hydrides are typically composed of cations (Li^+, Na^+, Mg^+, etc) and the hydrogen containing group is typically a complex anion ([NH_2^-, [AlH_4^-], [AlH_6^{3-}], [BH_4^-]. In order for

Table 1.2: Examples of decomposition of Ternary hydrides

Reaction		$\Delta H^{formation}$ (kJ/mol)
$2LiH + Mg(NH_2)_2$	$\rightarrow Li_2Mg(NH)_2 + 2H_2$	41.6 [20, 21]
$6Mg(BH_4)_2$	$\rightarrow MgBH_{12}H_{12} + 5MgH_2 + 13H_2$	29.3 [22, 23]
$LiH + LiNH_2$	$\rightarrow Li_2NH + H_2$	66 [24]

the material to qualify, it should have a desorption enthalpy in the narrow range of 25-40 kJ/mol. Thermodynamic data are available for many of these reactions, and a few are listed in the Table 1.2. For those that do not meet the thermodynamic criteria, typically little can be done to improve them, however kinetics of reactions can be modified. Many of these reactions have the caveat that they are kinetically limited, and must undergo a catalyzing process to improve kinetics.

1.4 Destabilization reactions

If a hydrogen storage material is to be seriously considered in fuel cell vehicle, one of the main requirements is for de-/rehydriding kinetics to deliver hydrogen fast enough to the PEM fuel cell gas chamber. Many catalytic additives, typically transition metals, are employed for improving kinetics [25–32] . Thermodynamics of a reaction however, such as the enthalpy of dehydrogenation cannot always be tuned for a desired range. It has been found that for reactions with excess enthalpy change, a number of additives can be employed destabilizing said reaction. Combining two hydrides forms a new compound, and a new set of products with overall lower energy. The starting phases are unchanged, and the overall enthalpy of reaction is lowered, which may be used for practical purposes.

Decomposition of Lithium borohydride is such an example. Pure $LiBH_4$ releases

about 13.8% mass of hydrogen with the following reaction

$$LiBH_4 \rightarrow LiH + B + 3/2H_2, \tag{1.3}$$

where the ΔH_{des} is given as 67 kJ/mol [33]. The desorption enthalpy can however be reduced to 46 kJ/mol in the following reaction

$$2LiBH_4 + MgH_2 \leftrightarrow 2LiH + MgB_2 + 4H_2, \tag{1.4}$$

This combination not only decreases the desorption temperature of $LiBH_4$, but actually improves reversibility by improving dehydrogenation kinetically. As a result, this has motivated a wealth of research on the subject. [33–40]

CHAPTER 2

Computational Methods

2.1 Density Functional Theory

In recent years, ab initio methods have become indispensable in materials research. Computational methods have been instrumental to both predicting and interpreting phenomena that could be verified by experimental work. A vast number of problems can be addressed with these methods, efficiently and rapidly predicting properties such as bond lengths of molecules, energies and structural parameters of crystals. The benefit of computational methods is investigation of natural phenomena beyond what can currently be probed by experiment by studying molecules and materials on a quantum mechanical level. The basic objective of solving an electronic structure problem is finding the ground state energy of the electrons in a system of arbitrarily arranged atoms [1]. To do this, the Schrödinger equation is solved:

$$\hat{\mathrm{H}}\,\Psi \;=\; \mathrm{E}\Psi, \tag{2.1}$$

where $\hat{\mathrm{H}}$ is the Hamiltonian, Ψ is the wave function and E is the eigenstate energy. However a very limited number of problems can be solved exactly. For most problems, approximations must be made in order to solve for the ground state

[1] For a general introduction to Density functional theory, the sources used are: [41–54],

energy. Modern computational methods generally approach this problem within the Born Oppenheimer approximation. This approach solves two independent wave functions, and removes the effect of the heavy nuclei from calculations of the electronic interactions. Methods for solving the ground state energy that use this approach are, among others, the Hartree-Fock (HF), which approximates Ψ as a single Slater determinant of single-particle wave functions and Quantum Monte Carlo methods. The Density Functional Theory (DFT) method has shown to be particularly fast yet efficient, and become the near universal method of solving the electronic structure problem. Aside from the Born Oppenheimer approximation, DFT also simplifies the Coulombic repulsion between electrons. The prescription for DFT is to treat electrons as independent particles interacting with a fictitious potential. DFT has become the popular choice for electronic structure calculations, not only because it is a computationally relatively inexpensive and efficient method, but it also has the capacity to handle up to thousands of electrons in a system.

2.1.1 Theoretical fundamentals

Since the Born-Oppenheimer approximation has already been applied, the only substantial quantum mechanical calculation to the total energy to be computed is the Coulomb interaction between atomic nuclei, the total electron energy, and the electron-ion interaction, calculated with pseudo potentials, which will be addressed later.

The remaining system is described by the following Hamiltonian for an arbitrary number, N, interacting electrons, and involving three separate contributions:

$$\hat{\mathrm{H}} = \hat{\mathrm{T}} + \hat{\mathrm{V}}_{\mathrm{ext}} + \hat{\mathrm{V}}_{\mathrm{ee}}, \tag{2.2}$$

where the kinetic energy operator is given as:

$$\hat{\mathrm{T}} = -\frac{1}{2}\sum_{\mathrm{j}=1}^{\mathrm{N}} \nabla_{\mathrm{j}}^2, \tag{2.3}$$

the electron-electron repulsion

$$\hat{\mathrm{V}}_{\mathrm{ee}} = \sum_{\mathrm{j}<\mathrm{i}}^{\mathrm{N}} \frac{1}{|\mathbf{r}_{\mathrm{i}} - \mathbf{r}_{\mathrm{j}}|}, \tag{2.4}$$

and finally the one-body operator is given as:

$$\hat{\mathrm{V}}_{\mathrm{ext}} = \sum_{\mathrm{j}=1}^{\mathrm{N}} \mathrm{v}_{\mathrm{ext}}(\mathbf{r}_{\mathrm{j}}). \tag{2.5}$$

Where atomic units have been set to $\mathrm{e}^2 = \hbar = \mathrm{m}_e = 1$, and respectively are the charge of an electron, Planck's constant, and the mass of an electron. As a result, all energies are given in Hartrees (with conversion factor: 1 H = 27.2114 eV) and all distances are given in Bohr radii ($a_o = 0.529$ Å).

Using the variational principle, the ground state energy is obtained by:

$$\mathrm{E}_0 \;=\; \min_{\Psi} \langle\, \Psi \,|\, \hat{\mathrm{H}} \,|\, \Psi \,\rangle \tag{2.6}$$

$$\text{s.t.} \langle\, \Psi \,|\, \hat{\mathrm{H}} \,|\, \Psi \,\rangle \;=\; 1. \tag{2.7}$$

where the minimization is performed over all antisymmetric N-particle wave functions. The wavefunction here, is written as $\Psi(\mathbf{r}_i, \sigma_i ..., \mathbf{r}_{\mathrm{N}}, \sigma_{\mathrm{N}})$, where $\mathbf{r}_i$ gives the position of the i^{th} electron in the system, σ_i gives the spin state as either up, $\uparrow$, or down, $\downarrow$. Furthermore, the wavefunction must obey a set of boundary conditions. Typical boundary conditions are defined such that for an atom or a molecule the

wavefunction goes to zero at infinite distances, and in a crystal, it is periodic in all ordered directions.

The quantity v_{ext} is the potential at a point $\mathbf{r}_i$, that in the absence of any externally applied fields, arises from the presence of the atomic nuclei. The explicit definition is given as

$$v_{ext}(\mathbf{r}_j) = -\sum_{j}^{N_{nuc}} \frac{Z_j}{|\mathbf{r}_i - \mathbf{R}_j|}, \tag{2.8}$$

where N_{nuc} is the number of nuclei present, Z_j the atomic number of the nucleus, j, and $\mathbf{R}_j$ the position. Computationally, the solutions to Eq. 2.6 are expensive, due to the fact that for every added electron, the dimensionality of Ψ increases by a factor of three in each dimension, and a factor of four if spin is accounted for. However Density functional theory allows for the efficient calculation of many-electron ground states by switching from treating the electronic wave function to the electron density. This significantly reduces the dimensionality of the problem from the 3N variables standard to a many-electron wavefunction problem to only 3 space variables. At a point $\mathbf{r}$ the electron density is defined as

$$n(\mathbf{r}) = n_e \sum_{\sigma} \int d\mathbf{r}_2 \ldots \int d\mathbf{r}_{n_e} |\Psi(\mathbf{r}_i, \sigma_1, \ldots, \mathbf{r}_{n_e}\sigma_{n_e})|^2. \tag{2.9}$$

From normalization it is required that:

$$\int n(\mathbf{r}) d\mathbf{r} = n_e. \tag{2.10}$$

This method significantly reduces computation time in systems of many electrons, as any number of electrons are described by only three spatial coordinates.

The Hohenberg-Kohn theorems validate the treatment with electron densi-

ties. The first Hohenberg-Kohn theorem establishes that the external potential is uniquely determined by the ground-state electron density, up to an additive constant. Many different wave functions can yield a specific density n($\mathbf{r}$) From here, the functional F[n] is defined as

$$F[n] = \min_{\Psi \to n} \langle \Psi \mid \hat{T} + \hat{V}_{ee} \mid \Psi \rangle . \tag{2.11}$$

The minimization is performed over all antisymmetric wave functions, which are the ones that will be considered here. The functional F[n] does not depend on an external potential, $V_{ext}(\mathbf{r})$, and it is considered to be universal. Furthermore, it is the same for a given density n($\mathbf{r}$) regardless of the problem at hand. By definition,

$$\langle \Psi \mid \hat{V}_{ext} \mid \Psi \rangle = \int d\mathbf{r}\ V_{ext}(\mathbf{r})\, n_0(\mathbf{r}), \tag{2.12}$$

which combined with Eq. 2.11

$$F[n_0] + \int d\mathbf{r}\ V_{ext}(\mathbf{r})\, n_0(\mathbf{r}) = E_0, \tag{2.13}$$

where E_0 is the ground state energy of the system, and $n_0(\mathbf{r})$ is the ground state density. This demonstrates that a certain density $n_0(\mathbf{r})$ fully determines V_{ext} up to an additive constant of energy.

The second Hohenberg-Kohn theorem states that the exact ground-state density is the one that minimizes the energy. By applying the variational principle to Eq. 2.13, one obtains

$$E_0 = \min_{n} \left\{ F[n_0] + \int d\mathbf{r}\ V_{ext}(\mathbf{r})\ n_0(\mathbf{r}) \right\}, \tag{2.14}$$

where the minimization is over all reasonable densities that satisfy Eq. 2.10.

Eq. 2.14 establishes not only that the ground-state densities yield the ground-state energy, but also that any density other than the ground-state, yields an energy higher than the ground-state energy. Thus the Hohenberg-Kohn theorems validate the Hamiltonian acting on a set of electron densities, instead of wave functions. The results produce the unique ground state energy of the system.

In principle DFT is a formally exact theory that offers a prescription for determining ground states. Given an external potential, $V_{ext}(\mathbf{r})$ and a known functional F[n] of the electron density the ground state of a system can easily be calculated by performing the variational minimization in Eq. 2.14. However the accuracy of DFT calculations applied to real systems hinges on the quality of the approximate density functional used. Systems with few electrons or simple electronic distributions yield exact solutions to the Schrödinger's equation and approximate functionals are unnecessary when exact solutions can be obtained. For most real systems, sophisticated modern functionals are employed in the DFT method for remarkably accurate results. Previous works have shown valuable data on atoms with bond lengths predicted within less than 1 nm, lattice constants of solids with less than 0.005 nm and molecular energies within 0.2 eV of average error [55–58].

Since in general, the exact expression for F[n] is not known, different methods have been applied to address this fact. The Thomas-Fermi model, which describes F[n] with a local approximation of the kinetic energy of a non-interacting electron gas, plus the Hartree energy, produces a major error when calculating the kinetic energy as a density functional. Even with corrections to the exchange-correlation energy of electrons, this approximation to the functional fails with errors beyond tolerance for many applications. Approaches to the functional with orbital-free DFT methods work in similar ways, approximating the kinetic energy with non-interacting particles and have recently grown in popularity. To date the Kohn

Sham formalism, which will be discussed in the following sections, is the most universally implemented method of electronic structure prediction.

2.1.2 Kohn-Sham DFT

In Kohn-Sham theory a fictitious potential, V_{eff} interacts with an electron wave function which is approximated with non-interacting electron orbitals, ϕ_i. In KS, this potential defines the system as

$$\left[-\frac{1}{2}\nabla^2 + V_{eff}(\mathbf{r})\right]\phi = \epsilon_i\phi_i(\mathbf{r}). \tag{2.15}$$

where ϵ_i is the energy eigenstate of the Kohn-Sham orbital ϕ_i. Using these orbitals, the electron density is written as

$$n(\mathbf{r}) = \sum_{i=1}^{n_e} |\phi_i(\mathbf{r})|^2. \tag{2.16}$$

It's worth noting that only one set of single particle equations Eq. 2.15, is required to solve the Schrödinger equation. The energy functional for the system in Eqs 2.3 through 2.5 is given by

$$E[n] = F[n] + \int d\mathbf{r} V_{ext}(\mathbf{r})n(\mathbf{r}), \tag{2.17}$$

where the value $A[n] = E[n] - \mu n_e$ is minimized, given that $n_e = \int d\mathbf{r}$ and μ is a Lagrange multiplier

$$\frac{\partial F[n]}{\partial n(\mathbf{r})} + V_{ext}(\mathbf{r}) = \mu, \tag{2.18}$$

Applying this method to the system described in Eq. 2.15,

$$\frac{\partial \mathrm{T_s[n]}}{\partial \mathrm{n}(\mathbf{r})} + \mathrm{V_{eff}}(\mathbf{r}) = \mu, \tag{2.19}$$

where $\mathrm{T_s[n]}$ is the kinetic energy of non-interacting electrons as expressed in the universal functional in Eq. 2.13.

$$\mathrm{F[n]} = \mathrm{T_s[n]} + \mathrm{E_H[n]} + \mathrm{E_{xc}[n]}, \tag{2.20}$$

where $\mathrm{E_{xc}[n]}$ is the exchange correlation energy and $\mathrm{E_H[n]}$ the Hartree energy, given by

$$\mathrm{E_H[n]} = \frac{1}{2}\int \mathrm{d}\mathbf{r} \int \mathrm{d}\mathbf{r}' \frac{\mathrm{n}(\mathbf{r}')\mathrm{n}(\mathbf{r})}{|\mathbf{r}-\mathbf{r}'|}. \tag{2.21}$$

Substituting the expression from F[n] from Eq. 2.20 into Eq. 2.18, thus taking the functional derivative of F with respect to the density, it follows that

$$\mathrm{V_{eff}}(\mathbf{r}) = \mathrm{V_{ext}}(\mathbf{r}) + \mathrm{V_H}(\mathbf{r}) + \mathrm{V_{xc}}(\mathbf{r}), \tag{2.22}$$

where the $\mathrm{V_{ext}}(\mathbf{r})$ term is the Hartree potential

$$\mathrm{V_H}(\mathbf{r}) = \int \mathrm{d}\mathbf{r}' \frac{\mathrm{n}(\mathbf{r}')}{|\mathbf{r}-\mathbf{r}'|}, \tag{2.23}$$

and the last time is the exchange-correlation potential

$$\mathrm{V_{xc}}(\mathbf{r}) = \frac{\partial \mathrm{E_{xc}[n]}}{\partial \mathrm{n}(\mathbf{r})}. \tag{2.24}$$

2.1.3 Exchange-Correlation Functionals

When the system is treated as non-interacting, the real natural interactions between the electrons are lost in the calculation. The exchange-correlation energy is a blanket term that accounts for the electronic interaction. Its exact definition is the difference between the exact kinetic and electron-electron energies, and the equivalent energies determined by the Kohn-Sham DFT treatment. This is written as

$$\mathrm{E_{xc}[n]} = \langle\, \Psi[\mathrm{n}] \,|\, \hat{\mathrm{T}} + \hat{\mathrm{V}}_{\mathrm{ee}} \,|\, \Psi[\mathrm{n}] \,\rangle - \langle\, \Phi[\mathrm{n}] \,|\, \hat{\mathrm{T}} + \hat{\mathrm{V}}_{\mathrm{ee}} \,|\, \Phi[\mathrm{n}] \,\rangle, \tag{2.25}$$

where $\Psi[\mathrm{n}]$ is the true wave function and $\Phi[\mathrm{n}]$ is the Kohn Sham wave function. Note the distinction, due to the fact that Kohn-Sham DFT generates the correct ground state electron density, however the associated orbitals are not the true ground-state wave function.

2.1.4 Local Density Approximation

The simplest and most common exchange-correlation model is the local density approximation. The first assumption is that the non-interacting electrons of the Kohn Sham model are allowed to move in a uniform electron gas of a net positive charge. Combined, the system has no charge. In such a construct, the exchange-correlation is given as:

$$\mathrm{E_{xc}^{LDA}[n]} = \int \mathrm{d}\mathbf{r}\, \mathrm{n}(\mathbf{r})\, \epsilon_{\mathrm{xc}}^{\mathrm{LDA}}[\mathrm{n}], \tag{2.26}$$

where $\epsilon_{\mathrm{xc}}[\mathrm{n}]$ is the exchange-correlation energy. It can be further divided into two parts

$$\epsilon_{xc}^{LDA}[n] = \epsilon_{x}^{LDA}[n] + \epsilon_{c}^{LDA}[n], \tag{2.27}$$

respectively, the exchange and correlation per particle.

$$\epsilon_{x}^{LDA}[n] = -\frac{3}{4}\left[\frac{3n(\mathbf{r})}{\pi}\right]^{1/3}. \tag{2.28}$$

while the exact expression for the correlation term is unknown, it can be derived from accurate quantum Monte Carlo calculations, for instance. Once the $\epsilon_{x}^{LDA}[n]$ is known, fits to the correlation energy can give analytic expressions to the correlation energy. For a uniform electron gas, the LDA method is exact, and can be applied to both slowly and rapidly varying densities. It is however still not chemically accurate, and more approximations are needed. The local spin-density approximation (LSDA) is a variant on the LDA model incorporating spins of electrons. This model is applied to systems that have an odd number of electrons, or systems that are spin polarized. In this case, the exchange-correlation energy is given as Eq. 2.27, but a functional with densities of both spin up and spin down electrons.

2.1.5 Generalized Gradient Approximation

The main feature of a model from a uniform electron gas is that the charge density is slowly varying. A basis for a model beyond this paradigm requires a higher-order correction to the exchange correlation energy. If the exchange correlation energy ϵ_{xc} is expanded in a Taylor series,

$$\epsilon_{xc}^{LDA}[n] = a[n] + c[n] \mid \nabla n \mid^2 + \ldots \tag{2.29}$$

the zeroth-order term is the local density approximation, and the linear term integrates to zero. Exchange-correlation energy is treated with only local densities in both the LDA and the LSDA method. The higher-order correction is the term with c[n], and this is employed in the gradient expansion approximation. [42]

The benefit of this approach is that it does not fit to reference data of atoms or molecules, rendering it completely from first principles. However a caveat of the gradient expansion approximation is that it does not obey physical rules. When the gradient correction is added the model for the hole that was derived from a physical system, the uniform electron gas, no longer behaves correctly. This behavior is particularly noticeable at large separations.

2.1.6 Bases and cutoff method

In the field of hydrogen storage, the materials that are of primary interest are metal hydrides, in other words, ordered structures. As has already been discussed, modeling those periodic structures requires periodic boundary conditions. The structure is constructed as infinite periodic arrays of nuclei, where the motion of electrons obey the Schrödinger equation as Bloch waves. These wave functions are given by

$$\Psi_{\mathrm{k}}(\mathbf{r}) = \mathrm{u}_{\mathrm{k}}(\mathbf{r})\, \mathrm{e}^{\mathrm{i}\mathbf{k}\cdot\mathbf{r}}, \tag{2.30}$$

where $\mathrm{u}_{\mathrm{k}}(\mathbf{r})$ is the Bloch function representing the magnitude of the periodicity of the lattice, and $\mathrm{e}^{\mathrm{irk}}$ is the plane wave where $\mathbf{k}$ is the wave vector. The basis set for the DFT calculations comes from the Kohn Sham orbitals that for a periodic, infinite system are written in Bloch wave form from Eqn. 2.30. Let the reciprocal space vectors be represented by $\mathbf{x}_1, \mathbf{x}_2$, and $\mathbf{x}_3$. The vector $\mathbf{G}$ connects equivalent sites on the lattice

$$\mathbf{G} = \mathrm{a}\mathbf{x}_1 + \mathrm{b}\mathbf{x}_2 + \mathrm{c}\mathbf{x}_3, \tag{2.31}$$

where a, b and c are integers. The Bloch function in Eqn. 2.30 can now be rewritten in terms of plane waves,

$$\mathrm{u_k}(\mathbf{r}) = \sum_{\mathbf{G}}^{\mathbf{G}_{\mathrm{cut}}} \mathrm{a_{k+G}}\, \mathrm{e}^{\mathrm{i}\mathbf{G}\cdot\mathbf{r}}, \tag{2.32}$$

and the Bloch waves are now given as

$$\phi_{\mathrm{k}}(\mathbf{r}) = \sum_{\mathbf{G}}^{\mathbf{G}_{\mathrm{cut}}} \mathrm{a_{k+G}}\, \mathrm{e}^{\mathrm{i}(\mathbf{k}+\mathbf{G})\cdot\mathbf{r}}. \tag{2.33}$$

Only valance electrons contribute substantially to interactions between the atoms. Thus they are of exclusive interest in quantum mechanical calculations, which will be discussed in the following section. Furthermore, it is known that far away from the nucleus, wave functions vary slowly. This is characteristic of plane wave functions oscillating with a small wave vector. The kinetic energy of a plane wave with a wave vector $\mathbf{k} + \mathbf{G}$ is given as

$$\mathrm{E} = \frac{1}{2} |\mathbf{k} + \mathbf{G}|^2. \tag{2.34}$$

A maximum energy, $\mathrm{E_{cut}}$ with a maximum wavevector, $\mathrm{G_{cut}}$ finds which plane waves are included in the calculations. Plane waves must satisfy the condition

$$\frac{1}{2} |\mathbf{k} + \mathbf{G}|^2 < \mathrm{E_{cut}}, \tag{2.35}$$

correspondingly, the criteria is defined for wavevectors as

$$|\mathbf{k} + \mathbf{G}| \leq \mathrm{G}_{\mathrm{cut}}. \tag{2.36}$$

Only wavevectors satisfying this condition will be included in the Fourier expansion of Kohn-Sham orbitals. These criteria truncate Eqn 2.33 into a finite summation.

2.1.7 Pseudopotential Method

As has already been noted in the previous section, the electrons primarily involved in interaction phenomena are those furthest from the nucleus. Valence electrons are the most pertinent to calculations of material properties. Typically they are known to have smooth wave functions, that are slowly varying and described by plane waves with small wavevectors and kinetic energies below the cutoff. Conversely core atoms are described by plane waves with large wavevectors, as they have rapidly varying wavefunctions in real space. When modeling valence electrons, it is desirable to remove core electrons and take advantage of functions featuring less rapidly varying oscillations. To do this properly, pseudopotentials are introduced. For a number of electrons within some cutoff radius, the electrons are replaced by an effective potential that is specifically designed to the correct value of valence electron density. The pseudopotentials interact with valence electrons via an operator. This operator ensures that the valence electrons behave as if all electrons were included in the calculation. [2]

[2]The following sources discuss the theory of pseudo potential methods, and their applications: [59–67]

2.1.8 Molecular dynamics calculations

Some calculations require not only the total energies, but also the net force acting on the atoms. This can be done very efficiently by taking advantage of the Hellmann-Feynman theorem [68].

$$\frac{\partial E_\lambda}{\partial \lambda} = \frac{\partial}{\partial \lambda} \langle \Psi \,|\, \hat{H} \,|\, \Psi \rangle = \langle \Psi \,|\, \frac{\partial \hat{H}}{\partial \lambda} \,|\, \Psi \rangle. \tag{2.37}$$

The Hellman-Feynman theorem relates the total energy derivative with respect to some parameter λ, to the expectation value of the derivative of the Hamiltonian with respect to the same parameter λ. In DFT calculations, and this work, the forces are thus simply obtained by taking the expectation value of the derivative of the Hamiltonian with respect to the atomic positions. Computational methods allow us to quickly and efficiently calculate the forces on all atoms in a given lattice. From these any problem of molecular structure involving intermolecular forces, such as valence bond stiffness, or distortions in geometry can be easily addressed. [69, 70]

2.2 Temperature and Pressure correction to the Free Energy

The relevant phenomena for hydrogen storage in metal hydrides often occur at temperatures that are much higher than ambient conditions. However, the DFT gives energy, therefore, observables at T= 0 K, and finite-temperature corrections are essential to reach meaningful predictions. At non zero temperatures, excitations in metal hydrides can take the form of electronic excitation, lattice vibrations and configurational disorder. Given that in metals the electronic excitation result

in fairly small entropies, the only solid-state excitations to be seriously considered are lattice vibrations. Free energies of gaseous H_2 are also calculated, which account for the effects of gas pressure on the lattice system as well.

2.2.1 Vibrational Free Energy

In a canonical ensemble[3], the partition function, Z is defined as

$$Z = \sum_{n} e^{-\beta E_n}, \tag{2.38}$$

where $\beta = (k_B T)^{-1}$, k_B is the Boltzman constant, T is the temperature, and the sum in Eq. 2.38 is taken over all states n, such that E_n is the energy of the n^{th} state.

To get the free energy term, $G = H - T\,S$, the enthalpy and the entropy are written in terms of the partition function as:

$$H = -\frac{\partial \ln Z}{\partial \beta}, \tag{2.39}$$

and

$$S = k_B \frac{\partial (T \ln Z)}{\partial T}, \tag{2.40}$$

The compound system is treated as a system of quantum mechanical harmonic oscillators, then the partition function is equal to

$$Z = \prod_{i=1}^{3N_{total}-3} \frac{1}{2\sinh(\beta \hbar \omega_i/2)}, \tag{2.41}$$

where $\hbar$ is the Planck constant, ω_i is the i^{th} vibrational frequency. The product

[3]adapted from sources: [71–78]

is taken over all optical frequencies, considering a system of N_{total} atoms.

The harmonic frequencies of a system are of interest, and they can be calculated by diagonalizing the dynamical matrix in

$$\omega^2 \mathbf{q} = \tilde{\mathbf{D}} \cdot \mathbf{q}, \tag{2.42}$$

where one element of the matrix is given as

$$D_{a\gamma a'\gamma'}(\mathbf{q}) = \frac{k_{a\gamma a'\gamma'}}{\sqrt{m_a m_{a'}}} e^{i\mathbf{q}\cdot(\mathbf{r}_{a'}-\mathbf{r}_a)}. \tag{2.43}$$

.

The masses of the atoms a and a' are m_a and $m_{a'}$, with positions $\mathbf{r}_a$ and $\mathbf{r}'_a$. The wave vector is given by $\mathbf{q}$. The force constant $k_{a\gamma a'\gamma'}$ updates the displacement of atom a' moving in direction γ' in accordance to a force on atom a in the direction γ. The Brillouin zone volume scales as the inverse of real space volume. This means that for large super cells variation in ω is small and the equations can effectively be evaluated at $\mathbf{q} = 0$ only. The method employed in this work calculates forces generated by the displacements that are inequivalent according to symmetry operations of the lattice, with the VASP program [52]. The forces are fit with a 3^{rd} order Chebyshev polynomial, and only two displacements on either side of equilibrium position is considered. The first order term only is taken from the force constant for a fit. Next the dynamical matrix is diagonalized and the harmonic frequencies in the system are obtained. Vibrational entropy and enthalpy are calculated according to Eqs. 2.39 and 2.40 from those harmonic frequencies. Additionally the zero-point vibrational energy is taken into account. For the most part, pressure effects are not considered, unless explicitly stated. The pressure

effects on solid phases are negligible in comparison to the pressure dependence of the entropy of gaseous H_2.

2.2.2 Free Energy of gaseous Hydrogen

The free energy of gaseous hydrogen has two separate terms, the energy and the entropy term. According to the equipartition theorem, the enthalpy per H_2 molecule increases by $\frac{1}{2}k_BT$ per degree of freedom [79]. Since H_2 is a diatomic molecule, it has three translational, two rotational, and one vibrational degree of freedom. Aside from the zero point energy, the vibrational mode can be neglected, as the temperatures at which the system is studied leaves this mode inactive. Hydrogen gas is further treated as an ideal gas, and the enthalpy increases by a unit of $pV = k_BT$, where p is the pressure, V is the volume, giving

$$H_{H_2} = \frac{7}{2}k_BT + H_{ZPE}. \tag{2.44}$$

Starting with the differential Gibbs free energy, $dG = Vdp - SdT$ the temperature, and pressure dependence of the H_2 entropy is calculated . The limit is taken with constant pressure, and it's trivial to show that $S(T) = \frac{7}{2}k_B \ln(T) + A_0$, where A_0 is a constant. In the limit of constant temperature, $S(p) = -k_B \ln(p) + B_0$, and B_0 is a constant. Experimental data is applied, where T = 300 K, p= 1 bar give a value of entropy as $S_{H_2} = 130.6$ kJ/(mol H_2). Thus the entropy of gaseous H_2 is given as,

$$S_{H_2}(T, p) = k_B \left(\frac{7}{2} \ln T - \ln p - 4.22 \right). \tag{2.45}$$

The total Gibbs free energy, $G = H - TS$ of gaseous hydrogen is given by com-

bining Eqn. 2.44 and 2.45

$$G_{H_2} = k_b T \left[\frac{7}{2}(1 - \ln T) + \ln p + 4.22 \right] + H_{ZPE} + H_{stat}. \tag{2.46}$$

Here, H_{ZPE} is the zero point vibrational energy of a single H_2 molecule. The value H_{stat} is the calculated electronic energy, from first principles, where it's assumed that $T = 0\,K$ in a periodic cell of dimensions $10\times10\times10$ Å.

CHAPTER 3

Mass transport in the dehydrogenation of the composite LiH + $LiNH_2$

3.1 Introduction

Up until the 2002 publication by Chen et. al [80], amides have not been thought of as viable hydrogen storage systems. Chen et.al demonstrated reversible storage of a large quantity of hydrogen in the LiH-$LiNH_2$ system. The interaction between the lithium amide and lithium hydride can be seen in Equation 3.1. In a reaction with lithium hydride, lithium amide decomposes into gaseous hydrogen and lithium imide. At higher temperatures the latter can decompose further into Li_3N, further releasing H_2 .

$$LiNH_2 + LiH \rightarrow Li_2NH + H_2, \tag{3.1}$$

$$Li_2NH + LiH \rightarrow Li_3N + H_2. \tag{3.2}$$

Individually the two metal hydrides are unremarkable as hydrogen storage materials. Hydrogen desorption in pure $LiNH_2$ does not occur until high temperatures of above 300 °C. Additionally, LiH is a highly stable hydride with a formation enthalpy of 91 kJ/mol, and only releases hydrogen above 600 °C [81,82]. However, the composite system LiH-$LiNH_2$ releases hydrogen at relatively low 180°C, with

a dehydrogenation enthalpy of 66 kJ/mol. [27]. The requirement for reversible on-board hydrogen storage is a dehydrogenation enthalpy range of 20-50 kJ/mol, so thermodynamically the composite system is still too stable to be practical [22]. It has also been found in temperature-desorption experiments that pure $LiNH_2$ releases ammonia (NH_3), which could damage a PEM cell, before any H_2 is desorbed [8], while the composite suppresses the ammonia release.

It has been found that transition metal, or their compounds, make good catalysts for hydrogen release in metal hydrides. Attempts have been made to bring down the dehydrating enthalpy of amide [22]. Some success has been gained with a mixture of $LiNH_2$ and MgH_2 [22], which was reported of having an experimental enthalpy of 39 kJ/mol [27]. In general, it is known that the enthalpy of dehydrogenation can be tuned with the addition of elements or metal hydrides, creating reactive hydride composites. This is an effective way of lowering the dehydrogenation enthalpy because it creates stable dehydrated products which are crucial to reversibility of the dehydrogenation reaction [27].

The features that distinguish the composite LiH-$LiNH_2$ system, are the non-metallic elemental N, the availability of both protic and hydridic hydrogen ($H^{\delta+}$ in $LiNH_2$ and $H^{\delta-}$ in LiH), and the high chemical potential resulting from the combination of protic and hydridic hydrogen to molecular hydrogen [83, 84].

$$H^{\delta+} + H^{\delta} = \Delta H \qquad\qquad \Delta H = -17.37\text{eV}, \tag{3.3}$$

The high chemical potential contributes to the driving force for total mass transport, resulting in improved thermodynamics.

The kinetics of the decomposition of metal hydrides into either intermediates and reaction products is quantified by the activation energy. Experimentally, the

activation energy for the decomposition of $LiNH_2$, or Reaction 3.1 was determined with thermogravimetric analysis, and the Johnson-Mehl Avrami analysis [85]. The activation energy for the dehydrogenation of $LiNH_2$ – LiH has been reported to be in the 128 -138 kJ/mol range [86, 87].

Recent experimental studies of synchrotron X-ray diffraction by David et al. [88] concluded the decomposition from $LiNH_2$ into Li_2NH is a non-stoichiometric bulk reversible reaction, facilitated by the migration of Li^+ and H^+ defects. The mechanism proposed involves formation of the intermediate ammonia, which then goes on to react with lithium hydride in a gas/solid reaction forming lithium imide, and releasing gaseous hydrogen [88]. For the second decomposition reaction, shown in Eq. 3.2, David et al. proposed that NH^{2-} unit of lithium imide forms $NH_2{}^-$ by interacting with protonic hydrogen, forming lithium hydride as well from the lone Li^+ defect. In this proposed scenario, the dehydrogenation would be driven by Li^+ and H^+ mobilities in disordered $Li_{1+x}NH_{1-x}$ phases [88]. However this particular kinetic pathways appears to be dependent on particle size. Morphology of samples (meaning average particle size and intermixing quantity) plays a key role. In the work of David et al. primarily large particles have been used, and it has been confirmed through diffraction techniques that all particles are 100 nm or larger. Recent theoretical calculations have investigated the thermodynamics [23] and kinetics of the ammonia-mediated route. These studies find that ammonia release becomes thermodynamically favorable at temperatures that are comparable to the critical temperature of Reaction 3.1.

For the case of small particles Chen et al. [89] proposed alternate mechanism where H_2 is created directly from the interaction between $LiNH_2$ and LiH, without an ammonia intermediate. Thoroughly mixed and combined, small lithium amide and lithium hydride particles will release H_2 via an interfacial solid-state redox

reaction.

Experimentally it has been shown that ball milling the samples of $LiNH_2$ – LiH [80] reduces the kinetic barrier. Ball milling not only efficiently reduces particle size, it also adequately mixes the samples thereby increasing contact between the amide and the lithium hydride in the compound mixture [27]. It has also been suggested by Hoang et al [90] that the limiting reaction for the dehydrogenation of Reaction 3.1 is facilitated by an intermediate NH_3 compound.

Computational methods involve rigorous theoretical analysis and insight beyond what is observable by today's experimental methods. Therefore they are excellent candidates for calculating values of atomic-level processes. The work here is modeled after an atomic-level first principles study of kinetics first pioneered by Gunaydin et. al [91] and later Michel et al. [92–94] for the decomposition of another hydrogen storage hydride, $NaAlH_4$. It has been found that the limiting process for the dehydrogenation of $NaAlH_4$ was the diffusion of Na vacancies through the Na_3AlH_6 diffusive phase. The methodology is comparable, and the aim to further the general knowledge on the atomic-level processes in the kinetic pathways of metal hydrides.

3.2 Methods

3.2.1 Morphologies

The physical arrangement of the reactants and products present in the reactions is referred to as the system morphology. A discussion of the morphologies is crucial to constructing a functional model of defect diffusion. Firstly, in order for the reaction to progress, it is assumed that all the phases in Reaction 3.1 are in

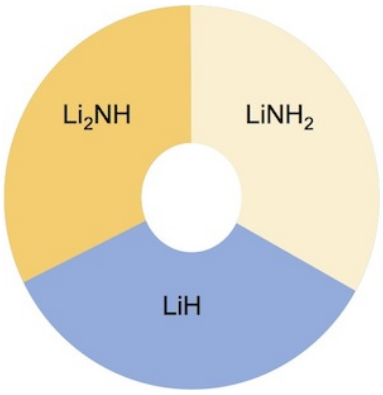

Figure 3.1: The possible morphologies in the $LiNH_2$ – LiH reaction.

contact. This can be visualized by a circular diagram in Figure 3.1.

The defects are created at each of the interfaces. Consequently, concentration gradients arise that drive general mass transport through each phase. The circular diagram is further broken down into 1D models, as seen in Figure 3.2. In each of these models defects travel through the center, or diffusive phase, and as the reaction progresses, said phase either grows in the case of dehydrogenation, or shrinks during rehydrogenation. The model is constructed to distinguish between the competing kinetic pathways, characterized by the phase that provides the mass transport mechanism: Li_2NH (Figure 3.2, top panel), $LiNH_2$ (Figure 3.2 middle panel) and LiH (Figure 3.2, bottom panel). In the bottom panel, defect flux is through the LiH phase, and since all of the $LiNH_2$ is used up in the reaction in order to produce Li_2NH, it is necessary for N species to diffuse through the LiH phase. However substituting an N atom at the LiH lattice is very costly in energy. It has been calculated here that the formation energy of N on LiH sites is high at both interfaces with Li_2NH and $LiNH_2$ (higher than 2 eV). Creating and diffusing N species in LiH is too costly, and it leads to insignificant fluxes in that particular morphology. Therefore the only two morphologies that need to be focused on are

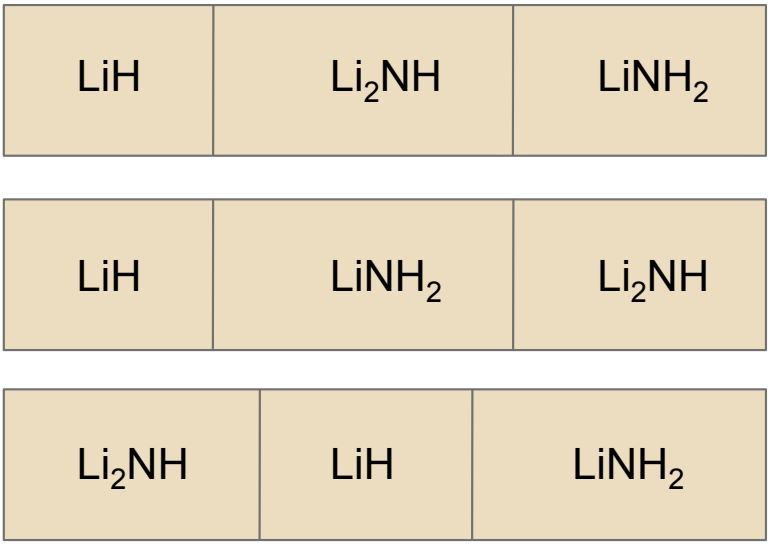

Figure 3.2: Linear schematic of the possible morphologies.

those with diffusion through Li_2NH and $LiNH_2$, in Figure 3.1, top and middle panel.

3.2.2 Activation energy and Arrhenius equation

Fick's law of diffusion is applied to all diffusing species in the system. Therefore, the flux of a defect i through either of the diffusive phases in Fig. 3.2 is defined as

$$\mathrm{J_i} = -\mathrm{D_i}\nabla\mathrm{C_i}, \tag{3.4}$$

where D_i is the diffusivity of the defect and $\nabla\mathrm{C}_i$ is the concentration gradient calculated between two interfaces. The concentration gradient provides the driving force for the reaction. Methods to calculate the gradient of the concentration will be discussed in the following subsections. In this work, the gradient is calculated over a distance of 1 μm. This choice is arbitrary, however it has been chosen

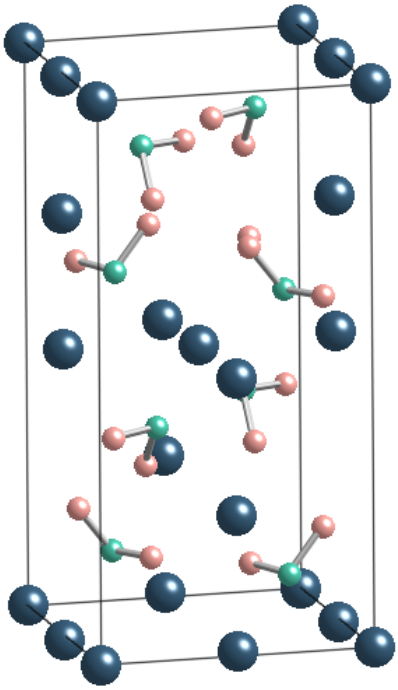

Figure 3.3: Unit cell of the $LiNH_2$ structure, Li ions in blue, NH_2 clusters in green/pink.

because ball milling of Li_2NH–LiH compound yields particle size in that dimensionality [80]. In experimental work, Arrhenius behavior is often assumed, and the fluxes are given as

$$J = J_0 e^{-E_A/k_B T}, \tag{3.5}$$

where J_0 is the Arrhenius pre-factor and E_A is the activation energy. The activation energy is the quantity that is experimentally measured via hydrogen desorption experiments [89]. The goal of this work is to find the activation barrier of each defect and match it to the experimental value found. The activation energy is

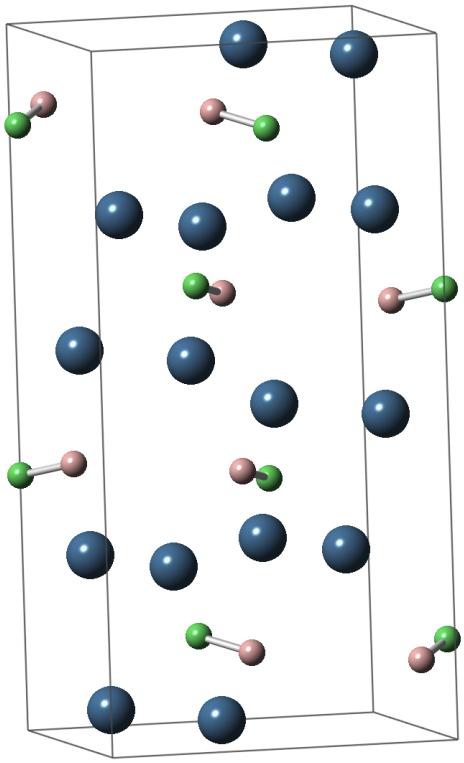

Figure 3.4: the unit cell of the Li_2NH structure, Li ions in blue, NH compound in green/pink.

defined as the sum of the energies required to create and diffuse a defect in bulk,

$$E_A = E_{form} + E_{mig} \,, \tag{3.6}$$

where E_{form} is the formation energy for each defect, and E_{mig} is the migration barrier. Comparing the sum of both values to the experimental activation energies yields the limiting factor in the process.

3.3 Results

3.3.1 Concentrations of Native Defects at Thermodynamic Equilibrium

It was assumed that the dominant mechanism for mass transport was the migration of native point defect in bulk phases. These were created based on what type of defects were thought as possible in the structures $LiNH_2$ (Fig. 3.3) and Li_2NH (Fig. 3.4). The types of defects created can be seen in Table 3.1 for the amide and Table 3.2 for the imide diffusive phase. The nomenclature in this work is such that $[X]^Y$ is a vacancy of a charge Y and ${}^iX^Y$ is an interstitial of charge Y. Oxidation states of Li (+1), (NH_2) (-1) were used to determine the charged state of defects. For instance $[NH_2]^+$ represents the NH_2 vacancy with a charged state of +1.

The equilibrium concentration of a single point defect is given as

$$C_i = \frac{D_i}{D_i + e^{\Delta E_i/k_B T}} \approx D_i e^{-\Delta E_i/k_B T}, \tag{3.7}$$

where D_i is the number of ways a particular defect can be introduced in the lattice, $\Delta\ E_i$ is the free energy of formation of a defect [95], as determined by

$$\Delta E_i = E_i(\text{defect}) - E_i(\text{supercell}) - \sum_s n_s^i \mu_s + q_i(E_{VBM} + \epsilon_F), \tag{3.8}$$

where E_i(defect) is the total energy of a supercell with the defect, E_i(supercell) is the energy of the perfect bulk supercell, n_s^i is the number of atoms of type s that are added ($n_s^i > 0$) or removed ($n_s^i < 0$) to create the defect, and the index s denotes the chemical potentials of atomic species determined by the experimental conditions. The electron chemical potential ϵ_F (i.e., the Fermi level) is referenced

to the valence-band maximum (VBM) E_{VBM} of the bulk material. In the following sections the methods used to evaluate terms of Eq. 3.8 are outlined. Concentration gradients, ∇C_i are calculated from differences in concentrations ΔC_i at each interface, divided by the distance between these interfaces.

3.3.2 Chemical potentials

The chemical potentials are crucial at the interfaces based on Fig.3.2. First mass transport through $LiNH_2$ is considered, or the middle panel in Fig3.2. The the relevant coexisting phases are $LiNH_2$, LiH, and H_2 at the left interface, and Li_2NH, $LiNH_2$ and H_2 at the right interface. The free energy equations at the interface between LiH and $LiNH_2$ are given by:

$$\begin{aligned} G(LiNH_2) &= \mu_{Li} + \mu_N + 2\mu_H, \\ G(LiH) &= \mu_{Li} + \mu_H, \\ G(H_2) &= 2\mu_H. \end{aligned} \tag{3.9}$$

where $G(LiNH_2)$ is the free energy of $LiNH_2$ including vibrational contributions. Additionally, $G(H_2)$ includes the the gas phase hydrogen energy discussed in Section 2.2.2. At the right interface, where $LiNH_2$ is in contact with Li_2NH, the free energies are

$$\begin{aligned} G(Li_2NH) &= 2\mu_{Li} + \mu_N + \mu_H, \\ G(LiNH_2) &= \mu_{Li} + \mu_N + 2\mu_H, \\ G(H_2) &= 2\mu_H. \end{aligned} \tag{3.10}$$

In the morphology of the top panel of Fig. 3.2 defects diffuse through the

Li_2NH phase. The present interfaces are now Li_2NH and LiH on the left, and Li_2NH and $LiNH_2$ on the right. The chemical potentials at the left interface must now satisfy

$$\begin{aligned} G(Li_2NH) &= 2\mu_{Li} + \mu_N + \mu_H \\ G(LiH) &= \mu_{Li} + \mu_H \\ G(H_2) &= 2\mu_H. \end{aligned} \tag{3.11}$$

The constraints on the chemical potentials at equilibrium, at each of the interfaces in the different morphologies result in chemical gradients between the interfaces. These chemical potential gradients result in fluxes that are responsible for the phase separation during the dehydrogenation Reaction 3.1. Combining the calculated DFT energies, and the vibrational contribution as discussed in Section 2.2.1 the equilibrium temperature, at P=1 bar H_2 pressure is calculated as T_{eq}^{DFT} = 395°C. The experimental value however is T_{eq}^{exp} = 180°C [27]. This temperature difference can significantly affect the concentration of defects, which have a strong exponential dependence on temperature, as seen in Eq. 3.7.

3.3.3 Fermi level

The Fermi level was determined from enforced charge neutrality. An example of how this occurs is, creating a positively charged defect in the lattice requires the creation of a corresponding negative defect. Two ways of calculating the Fermi level involve either enforcing charge neutrality separately at each interface, or allowing defects to equilibrate throughout the diffusive phase. The consequence of the first method is that a Fermi level gradient arises, and in the second it is held

constant. The condition that sets up charge neutrality is given as

$$\sum_{\mathrm{i}}^{\mathrm{N_{defects}}} \mathrm{C_i q_i} = 0. \tag{3.12}$$

In this work across all results, the first method has been applied, and charge neutrality is enforced at each interfaces. While the second method yields somewhat different quantitative results, qualitatively the two methods are similar.

3.3.4 DFT Calculations

All calculations were performed using DFT software VASP [53]. The generalized gradient approximation to the exchange-correlation functional was used [96]. Defects were introduced into bulk crystals with periodic boundary conditions, where in the pure phases $LiNH_2$ (and Li_2NH) contained 128 atoms each. This corresponds to dimensions in the supercell of $2a \times 2a \times 1c$ ($2a \times 1b \times 1c$), where a, b and c are lattice parameters from the conventional cell. The calculated band gap (3.5 eV) is consistent with previously published first-principles data [97]. $LiNH_2$, as seen in Figure 3.3, belongs to the tetragonal $I\bar{4}$/a space group For $LiNH_2$, the computed lattice parameter values of $a = 4.97$, $b/a = 1.0$ and $c/a = 2.00$ agree well with the experimental data of a=5.04, b/a=1.0 and c/a=2.04.19 [98]. Li_2NH, from Figure 3.4 belongs to the orthorhombic *Pbca* space group. The calculated lattice parameters are given as $a = 5.11$, $b = 10.50$ and $c = 5.26$, and they agree well with experiment [99]. Once the defects were introduced into the bulk, the structures were relaxed with respect to the atomic positions until residual forces were smaller than 0.01 ev/Å, while the cell shape and volume were fixed, following similar work of other authors [90, 91, 100].

Potentials were used with a cutoff energy of 250 eV. For accurate defect energies

in $LiNH_2$, the k-point mesh sampling was set to $2 \times 2 \times 2$ Monkhorst-Pack mesh. For Li_2NH, identical k-point settings were employed, while LiH was treated in a $4 \times 4 \times 4$ supercell with 128 atoms and a $2 \times 2 \times 2$ Monkhorst-Pack mesh. To prevent divergence in the Coulomb energy, the total number of charged states was set manually by adding a uniform, compensating background charge.

In the finite sized supercells a shift in the electrostatic potential is needed to move the Valence Band Maximum (VBM) to the supercell containing defects [101] However this shift has been found to only amount to 10-20 meV in $LiNH_2$. This term has been deemed practically negligible and excluded from the calculations in this work.

For the migration energies, it is necessary to find correct diffusion paths through the lattice. The diffusion paths of defects were determined using the Nudged Elastic band method [102]. This method requires two energetically relaxed structures at the endpoints of the diffusion path. Between the two endpoints, on the direct path, several new structures (referred to as images) are linearly extrapolated. The intermediate images will shift during diffusion to describe the manner in which the structure, or particular defect travels between endpoints. A spring force connects all of the images. The endpoints are fixed during minimization, while the images are relaxed under the constraint of the spring force. The perpendicular component of the spring force is ignored, and the components projected along the path determine the coordinate changes to the images, which eliminates the "corner-cutting" problem of general elastic band calculations. After the diffusion path is established, a more accurate method for finding the saddle point, or the transition state, is applied, the climbing image nudged elastic band (cNEB). This method disconnects the spring force from the image with the highest energy, and the calculated force is projected onto the path between the images. This component of

the force is inverted, and the image is pushed toward the true transition state. The migration barrier ΔH^{mig} in Eq. 3.6 for the activation energy, is the difference between the energy of this transition state, and the image from the initial configuration at the endpoints. Migration paths within the lattice are, for the most part, obvious choices. Nearest neighbor jumps are defined as complete diffusion paths, provided they allow for actual mass transport. For instance a vacancy, $[H]^+$ in $LiNH_2$ must travel the closest path between neighboring N-complexes in order to diffuse, as can be seen in Figure 3.3, where each N-complex is depicted by a ball and stick model, such that N are the green, and H the pink atoms.

For defects where such a path is not obvious, for instance defects involving interstitial sites, AIMD simulations were carried out. These simulations were run for about 10 ps, at T = 500 K (controlled using Nosé-Hoover thermostat). Once a jump was observed, snapshots of the lattice were taken before and after the event. The snapshots were relaxed energetically, and defined the endpoint structures for the NEB method calculations.

Zero-point corrections to the free energies were computed with the method discussed in Section 2.2. Vibrational modes were calculated in $LiNH_2$ and Li_2NH in supercells of 128 atoms for both cases. Only the real frequencies were used for the transition states and all the frequencies for the minimum energy structures.

3.4 Results

3.4.1 Native Defect Energies and Concentrations in $LiNH_2$

The formation energies including all temperature corrections are listed at 500 K in Table 3.1. At this temperature, the defects with the lowest formation free energy

at the LiH/$LiNH_2$ interface are for lithium vacancies (0.33 eV) and lithium on hydrogen site substitutions Li_H (0.26 eV). At the $LiNH_2$ / Li_2NH interface, the defects with the lowest free energies are the neutral NH vacancy, [NH] and Li_H. The table also shows the formation enthalpies of each defect. Comparing ΔG and ΔH gives the magnitude of entropic contribution. It is obvious looking at the defects that the free energies of defects are crucial. It is important to include the fee energy correction to gaseous H_2, since free energies are dependent on this correction.

In Fig. 3.5 the free energies of formation of the lowest-energy defects chosen from the ones in Table 3.1, are plotted against inverse temperature. At low temperatures, around 300 K, the neutral NH vacancy dominates at both interfaces. At higher temperatures, at around 500 K, the Li_H substitution becomes significant energetically. At really high temperatures, close to 600 K, at the $LiNH_2$ / Li_2NH interface it becomes energetically more favorable to create lithium species, both interstitial and vacancies, than the $[NH]^0$ defect.

Using the energies listed in Table. 3.1, the concentrations at 500 K, calculated from Eq. 3.7 are also listed. The number of ways to introduce defects into the lattice, which is given as D_i in Eq. 3.7 is 1 for most defects. There are 4 separate ways of introducing the lithium interstitial, which will coordinate with the $[NH]^{2-}$ ion in either a tetrahedral or octahedral position. Therefore, D = 1 for the defects with the lowest energies, which are then also the defects with the largest concentrations. At both the $LiNH_2$ / Li_2NH and the LiH/$LiNH_2$ interface, neutral NH vacancies and Li_H substitution defects have the highest concentrations within an order of magnitude of each other. The concentrations of the other defects are at least another order of magnitude smaller at this temperature.

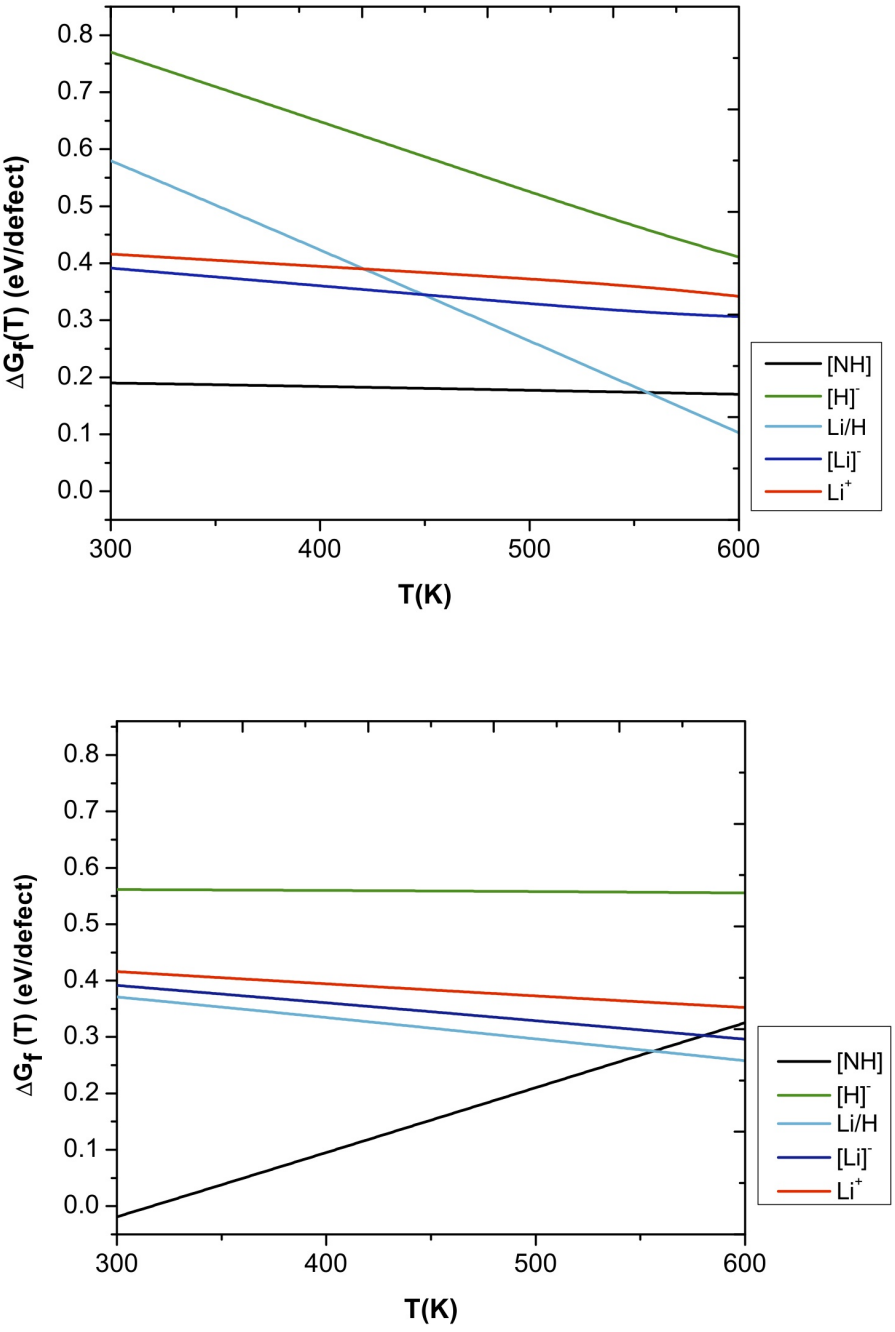

Figure 3.5: Free energies of defects in $LiNH_2$ formed at the $LiH/LiNH_2$ interface (top) and the $LiNH_2$/ Li_2NH interface (bottom).

Table 3.1: The free energies and concentrations (number of defects per f.u.) of all defects in $LiNH_2$ at 500K

Defects	$LiH : LiNH_2 : H_2$ [c]			$LiNH_2 : Li_2NH : H_2$ [d]		
	ΔH_{500K} [a]	ΔG_{500K} [a]	C_{500K} [b]	ΔH_{500K} [a]	ΔG_{500K} [a]	C_{500K} [b]
$[Li]^-$	0.286	0.329	9.57×10^{-4}	1.023	0.328	9.68×10^{-4}
$[H]^-$	1.070	0.525	4.03×10^{-5}	1.102	0.558	1.902×10^{-5}
${}^{i}Li^{+}_{\text{tetra 1}}$	0.706	0.372	7.04×10^{-4}	-0.031	0.3729	6.971×10^{-4}
${}^{i}Li^{+}_{\text{tetra 2}}$	0.845	0.601	3.48×10^{-6}	0.108	0.6017	3.448×10^{-6}
${}^{i}Li^{+}_{\text{tetra 3}}$	0.713	0.423	2.14×10^{-4}	-0.024	0.4241	2.126×10^{-4}
${}^{i}Li^{+}_{\text{octahedral}}$	0.864	0.469	7.49×10^{-5}	0.127	0.4694	7.417×10^{-5}
${}^{i}H^{+}_{\text{tetrahedral}}$	1.082	1.34	6.22×10^{-14}	1.115	1.372	2.931×10^{-14}
Li_H	1.201	0.2605	4.38×10^{-3}	0.497	0.297	2.044×10^{-3}
$[NH]^0$	0.237	0.177	3.21×10^{-2}	-0.467	0.210	1.51×10^{-2}
$[NH_2]^+$	1.083	0.764	1.97×10^{-8}	0.3457	0.765	1.944×10^{-8}

[a] In units of eV/Atom
[b] Number of defects in f.u. per
[c] For the interface between solid state LiH / $LiNH_2$ and gaseous H_2
[d] For the interface between solid state $LiNH_2$ / Li_2NH and gaseous H_2

In Fig. 3.6 the concentrations are given at both interfaces as functions of temperature. At the LiH/Li_2NH interface the highest concentration of defects at low temperatures is for the neutral NH vacancy, [NH]. Above 500 K the defects with the highest concentrations are the neutral [NH] and the lithium at hydrogen site, Li_H substitution. At the $LiNH_2$ / Li_2NH interface, there is a similar trend, with [NH] defects having the highest concentration by a few orders of magnitude at low temperatures, and at high temperatures, there is a combination of [NH] and Li_H as well as the charged $[Li]^-$ and the Li^+. Over a large range of temperatures, $[Li]^-$ and Li^+ compensate each other, having equal concentration, until they split apart at about 500 K. The interesting features is that the [NH] vacancy decreases in concentration with increasing temperature at the $LiNH_2$ / Li_2NH interface. This is because the formation free energy of the [NH] defect actually increases with temperature, because at high temperatures, [NH] is unstable in the Li_2NH phase. This data would suggest that above temperatures of 500 K the [NH] vacancies are formed at the LiH/$LiNH_2$ interface and diffuse across the $LiNH_2$ phase. This is also the equivalent of lithium hydride diffusing from the LiH/$LiNH_2$ towards the $LiNH_2$ / Li_2NH interface, where two units of lithium are required for every [NH] consumed to form Li_2NH. The process of diffusing the [NH] vacancy is an energetically costly one. Here it was calculated the diffusing [NH] requires more than 190 kJ/mol. Thus though the formation energy is low for this defect, it would not be the rate limiting process, since it is significantly higher than the expermentally observed value of 128 kJ/mol [21].

The concentration gradients of defects calculated between the interfaces, at a distance of d=1μm are given in Fig. 3.7. The species with large gradients are

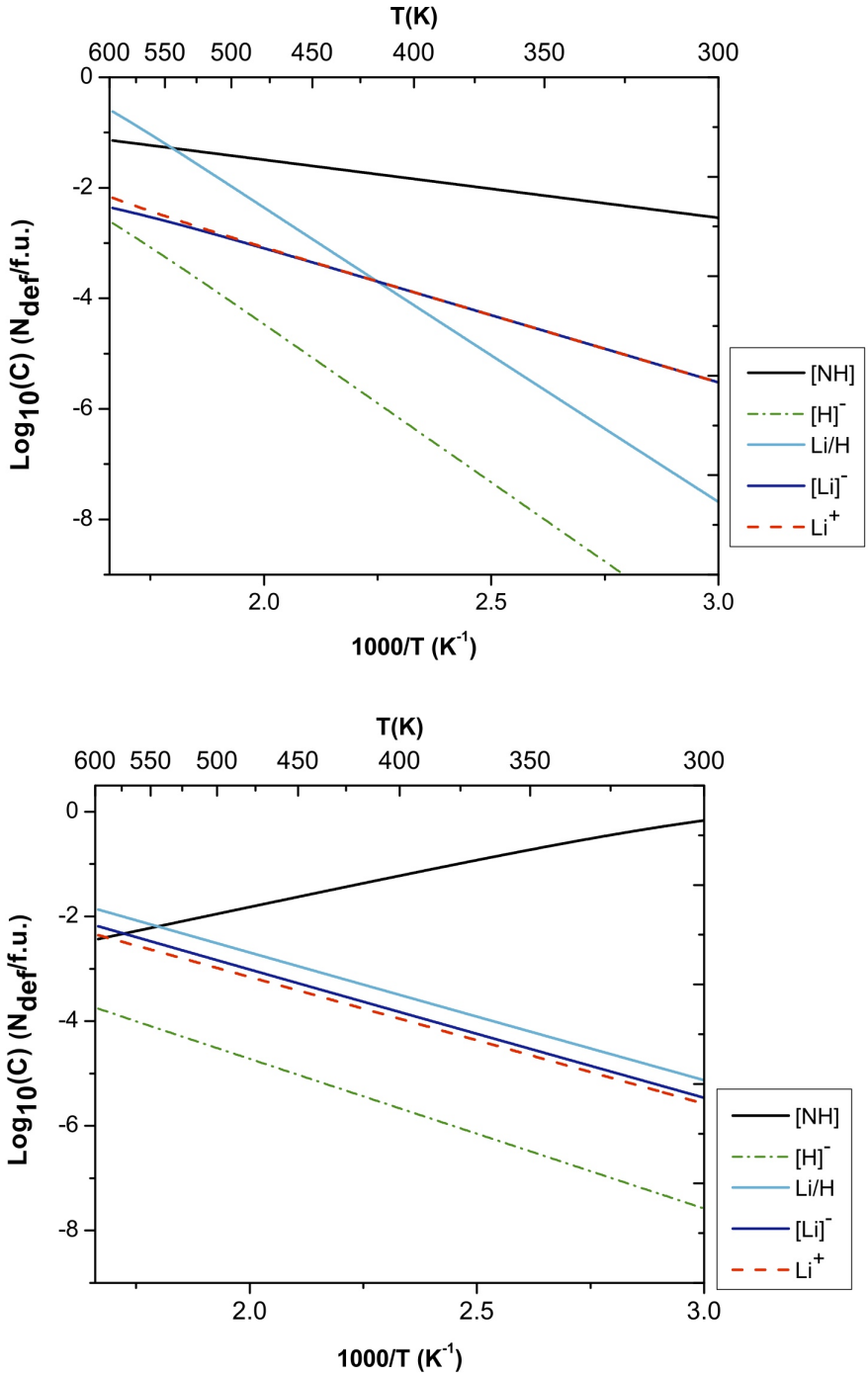

Figure 3.6: The temperature dependence of concentrations of defects in $LiNH_2$ formed at the $LiH/LiNH_2$ interface (top) and the $LiNH_2$/ Li_2NH interface (bottom). Defects of the highest concentrations are shown.

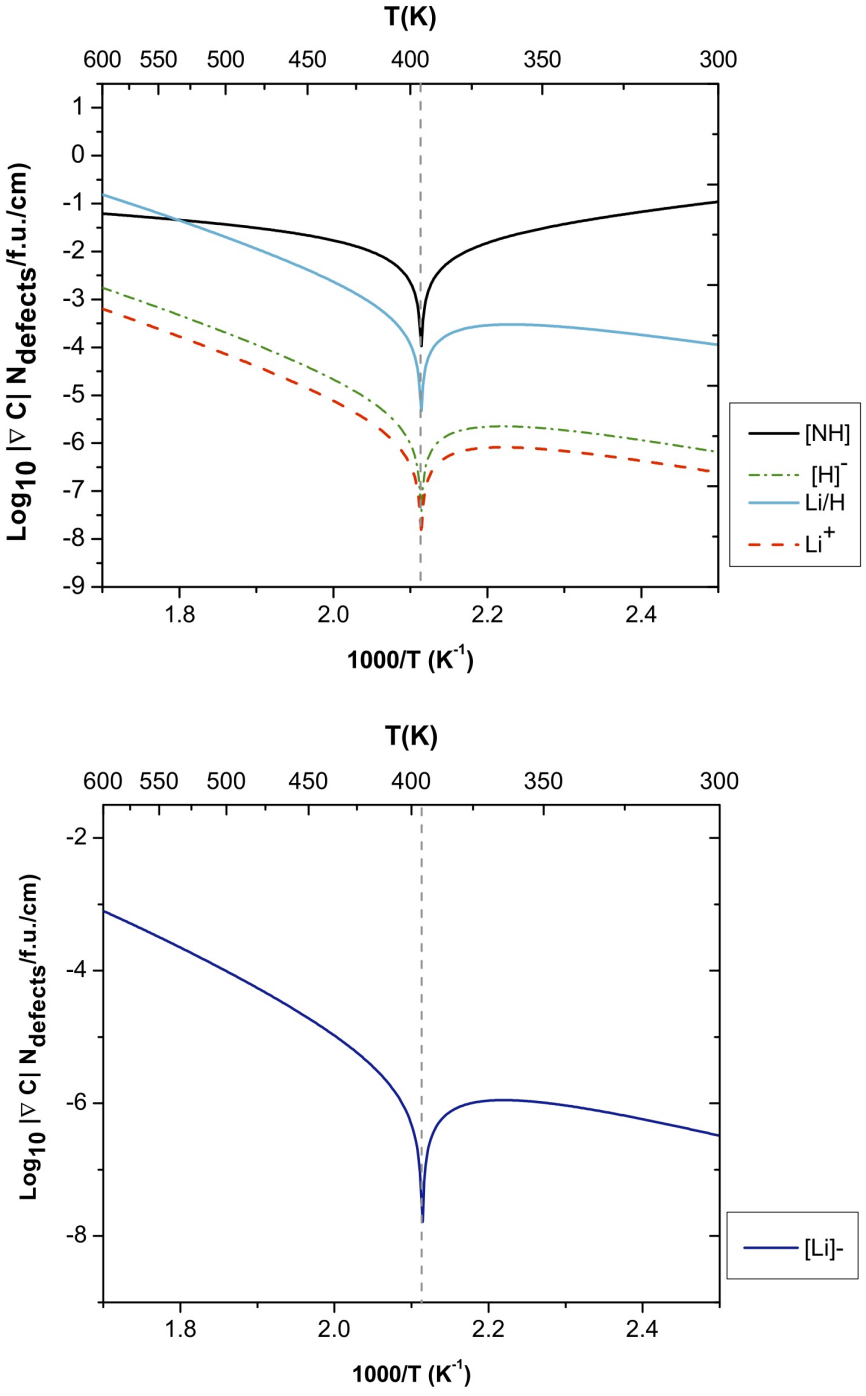

Figure 3.7: Concentrations gradients of defects in $LiNH_2$ moving toward the $LiH/LiNH_2$ interface (top) and moving toward the $LiNH_2$/ Li_2NH interface (bottom) during dehydrogenation.

mostly the NH vacancy and some Li containing species. It's also found that negatively charged hydrogen vacancy has a high gradient. The chemical potential of H is the same at both interfaces, and the large concentration gradient arises from different Fermi levels at the interfaces. In Fig. 3.7 there are three temperature regions that denote different phenomena. Looking at the top panel, the defects in this plot all move toward the same interface during dehydrogenation and rehydrogenation. At low temperatures [NH] vacancies move toward the Li_2NH phase, while Li vacancies move toward the LiH phase. This corresponds to the scenario in which Li_2NH is consumed, and dehydrogenation occurs in the amide phase. The equilibrium temperature is denoted by the gradients going toward zero. At this point, all free energies are equal, and no driving force is present to move mass transport in either direction. Then at high temperatures, in the top panel [NH] vacancies migrate toward the LiH phase from the Li_2NH. Conversely negatively charged Li vacancies move toward the Li_2NH phase. This scenario corresponds to the phenomenon of dehydrogenation of $LiNH_2$. With the exception of equilibrium temperatures, the concentration gradient is opposite in direction to [NH] vacancies and Li vacancies. At low temperatures it can either be viewed as Li vacancies are forced toward Li_2NH, or that Li interstitials are forced toward $LiNH_2$, while the product phase is consumed. Conversely at high temperatures, the gradient is reversed and the reactant phases, $LiNH_2$ and LiH are consumed.

3.4.2 Temperature Corrections to the Free Energy

Temperature corrections as discussed in Section 2.2 tend to be neglected in calculations of this kind, and it is important to explain their effect. Though these

calculations are expensive and complicated, including them means that the formation of defects can be more accurately studied as a function of temperature. In order to understand how these free energy corrections contribute to the energy the Fermi level is plotted against the temperature, shown in figure 3.8 when all corrections, the vibrational contribution, and the free energy of the H_2 gas phase is included.The inset panel within the plots indicates the diffusive phase for those plots. The dependence on temperature of the Fermi level is given at both interfaces, it increases by as much as 250 meV in both phases over the temperature range at the LiH/$LiNH_2$ interface. The static values of the Fermi levels in $LiNH_2$ are given as $\epsilon_F = 1.25$ eV at the LiH/$LiNH_2$ interface, and $\epsilon_F = 1.77$ eV at the $LiNH_2$ / Li_2NH interface. Comparing those values to the plot, at 500 K, the Fermi level at the LiH/$LiNH_2$ interface increases by more than 1 eV, compared to the Fermi level at the same temperature when only static, DFT energies are included. At the $LiNH_2$ / Li_2NH interface, the increase is equally significant at this temperature. It is also known that including the two temperature corrections to the free energy have a higher impact [100] than other corrections such as the electrostatic potential between periodic images, or the alignment of the valence band maximum in super cells with defect, to those in pure cells.

3.4.3 Native Defect Energies and Concentrations in Li_2NH

Let's consider the morphology in which defects are considered to diffuse through Li_2NH. The defect types considered in Li_2NH are negatively charged lithium vacancies, $[Li]^-$ (on two distinct sites), negatively and positively charged hydrogen vacancies $[H]^-$,$[H]^+$, positively charged lithium interstitials ${}^{i}Li^+$, negatively and

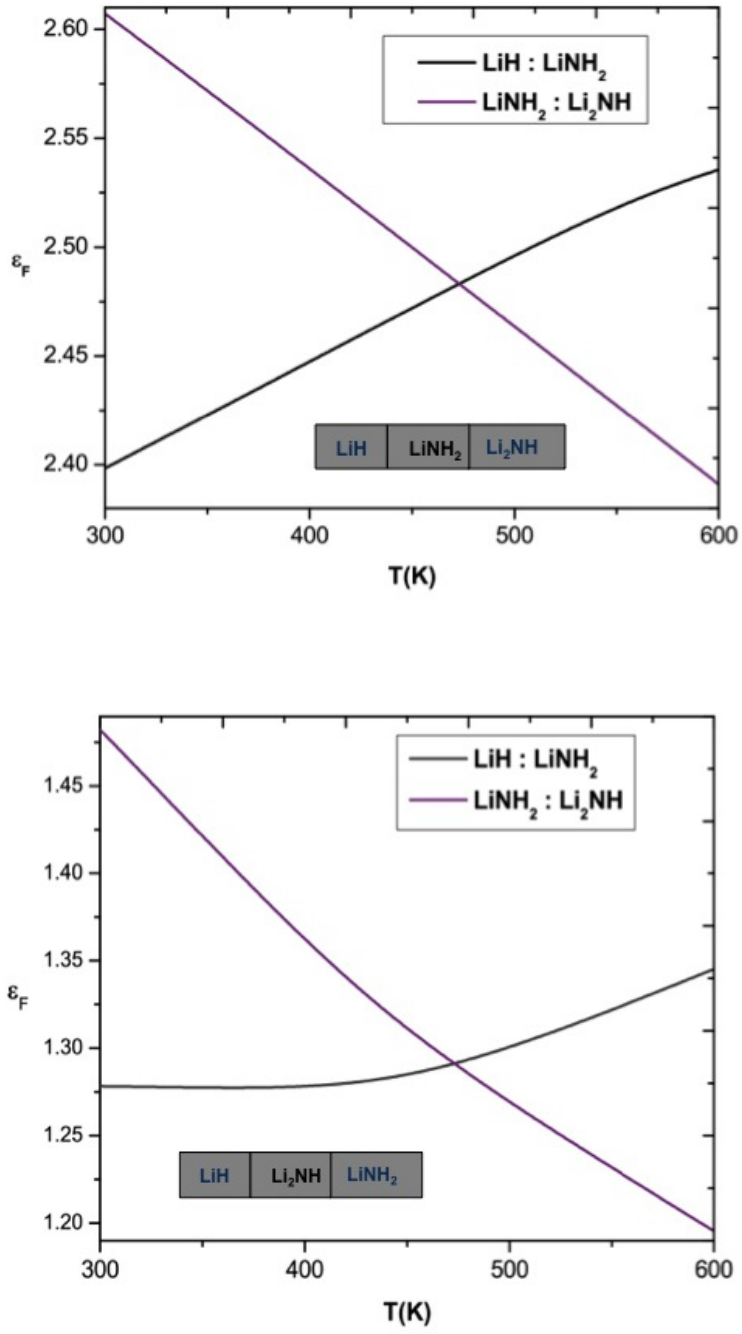

Figure 3.8: The Fermi levels area plotted against the temperature, in the $LiNH_2$ (top) and Li_2NH (bottom).

positively charged, as well as neutral hydrogen interstitials ${}^{i}H^{+}$, ${}^{i}H^{-}$, ${}^{i}H^{0}$, hydrogen substitutions on lithium sites, H_{Li} (on two distinct sites), positively charged lithium substitutions on hydrogen sites, neutral NH vacancies $[NH]^{0}$, and positively charged nitrogen vacancies, $[N]^{+}$.

The free energies of formation per defect are shown in figure 3.9, plotted against the temperature. All corrections of vibrational contribution and H_2 gas phase are included with the DFT energies. Across the plotted temperature range of T = 300 K to T = 600 K it can be seen that the Li vacancy is the defect with the lowest formation energy. In the $LiNH_2$ at very low temperatures, the H_{Li} substitution defect forms somewhat easier than the Li vacancy. At high temperatures, the Li vacancy is paired with a positively charged Li interstitial. At the Li_2NH/ $LiNH_2$ interface and low temperatures the Li vacancy is complemented with a negatively charged N vacancy. The lithium vacancy increases linearly with temperature, but the $[N]^{-}$ is the more interesting defect here. While at the LiH/Li_2NH interface the nitrogen vacancy increases linearly with temperature, at the Li_2NH/ $LiNH_2$ interface it behaves more nonlinearly. From about 300 K it slightly goes up in concentration, and then drops off again past the dehydrogenation. This can be attributed to the increase in free energy of the defect observed at the Li_2NH /$LiNH_2$. The positively charged N vacancy can be thought of as a negatively charged H^{-} taking the place of the NH^{2-} dimer upon the removal of N. At high temperatures, above 500 K, the same behavior is observed as at the other interface, namely the combined charge compensating lithium vacancy and lithium interstitial concentrations.

Concentrations of defects in Li_2NH at both interfaces, Temperature of 500 K

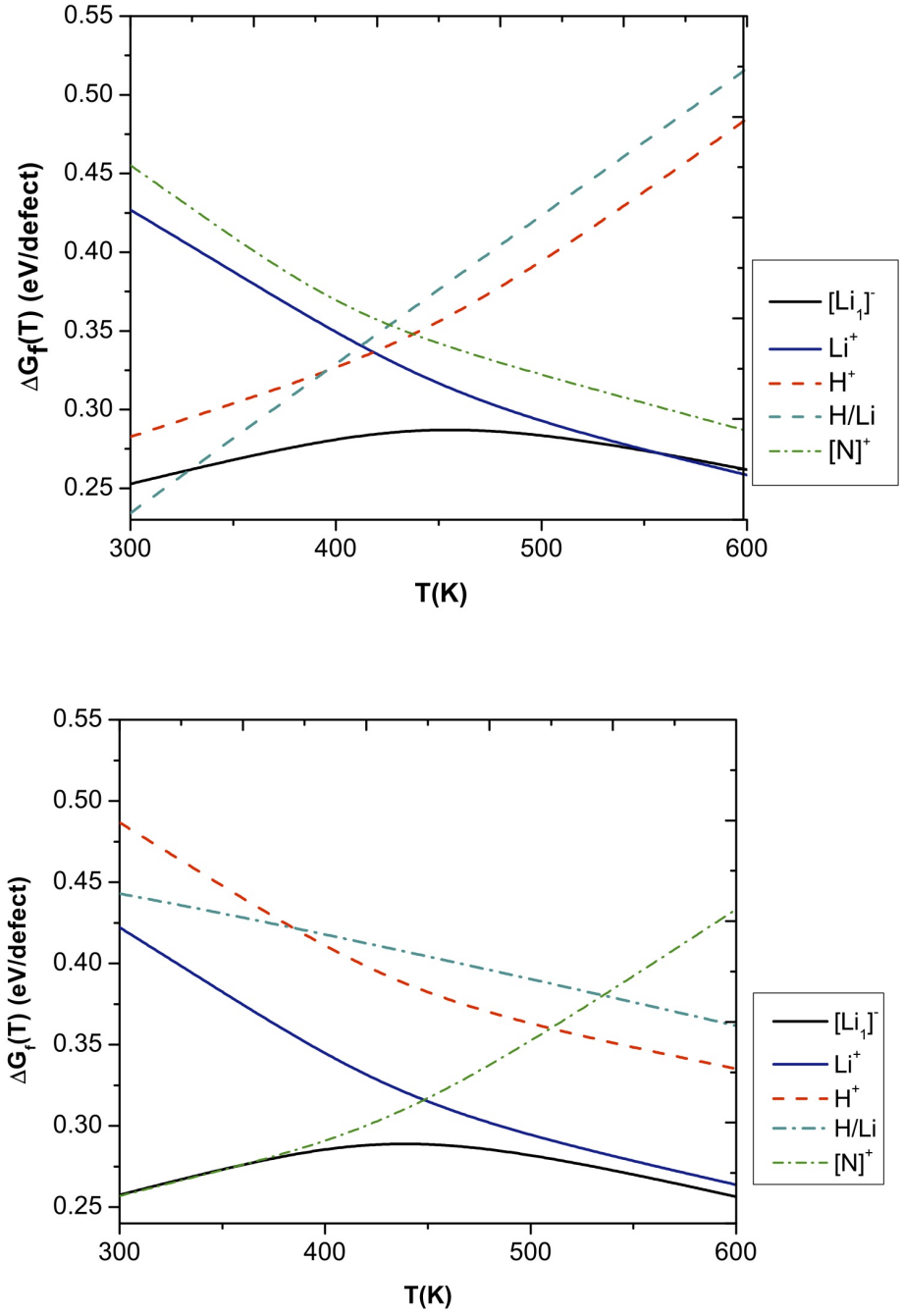

Figure 3.9: The Free energies plotted against temperature, at LiH/Li_2NH (top) and Li_2NH/ $LiNH_2$ (bottom).

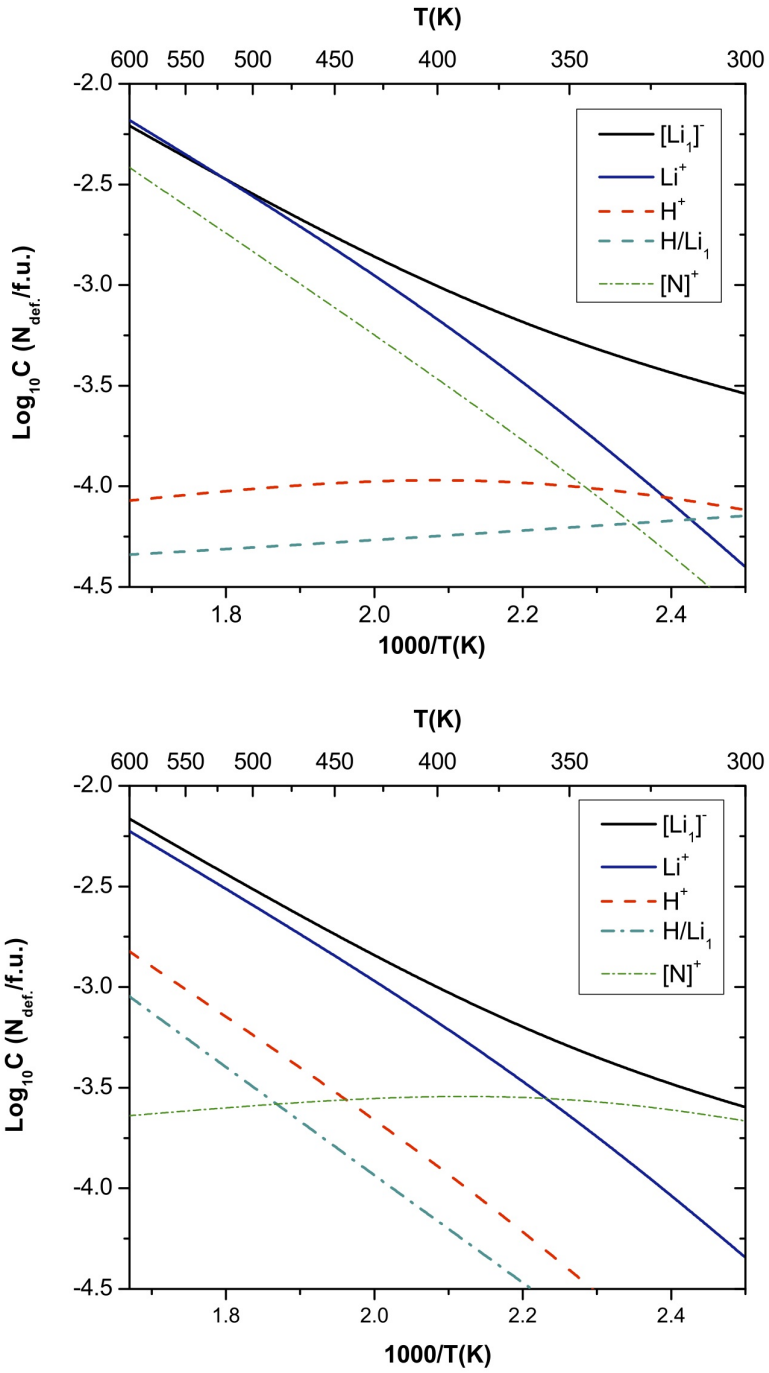

Figure 3.10: The temperature dependence of concentrations of defects in Li_2NH formed at the LiH/Li_2NH interface (top) and the $Li_2NH/\ LiNH_2$ interface (bottom). Only defects with the highest concentrations are shown.

and pressure of 1 bar, are given in Table 3.2 . The temperature dependence of these defects is shown in Figure 3.10. The value of D_i in Equation 3.7 is 1, therefore the highest concentrations correspond to the defects with lowest formation energies. These data show that the temperature dependence of defect concentrations can be highly complex and non linear, due to complex interactions of charged defects via the common Fermi level. This can be attributed both to the extensive change in formation energy with temperature, as is seen in Figure 3.9 and the Boltzman Factor, k_BT. At high temperatures, the charge compensating defects are the Li vacancy and interstitial, at both interfaces.

Finally, the concentration gradients of the defects transported in the Li_2NH phase, are given in 3.11 for d = μm. In the top panel, the defects move from the $Li_2NH/LiNH_2$ interface toward the LiH/Li_2NH interface as the reactant is consumed. The positively charged H interstitial has a high gradient at high temperatures, during which dehydrogenation occurs. The H interstitial moves away from the lithium rich phase and toward the interface with the LiH. Conversely, during dehydrogenation, these defects, the H interstitial, Li vacancy and H_{Li} substitution move toward the lithium rich interface. At the same time, defects in the bottom panel move in the exact opposite way. At high temperatures the positively charged N vacancies move toward the $Li_2NH/LiNH_2$ interface, while the $LiNH_2$ is being consumed during dehydrogenation. The magnitudes of the concentration gradients gives some intuitive insight into the mechanism of mass transport for Reaction 3.1. The magnitudes of the gradients for the Li_2NH phase were somewhat smaller than those for $LiNH_2$, therefore comparing concentrations of defects across both phases with the same width, it can be assumed that the gradients in

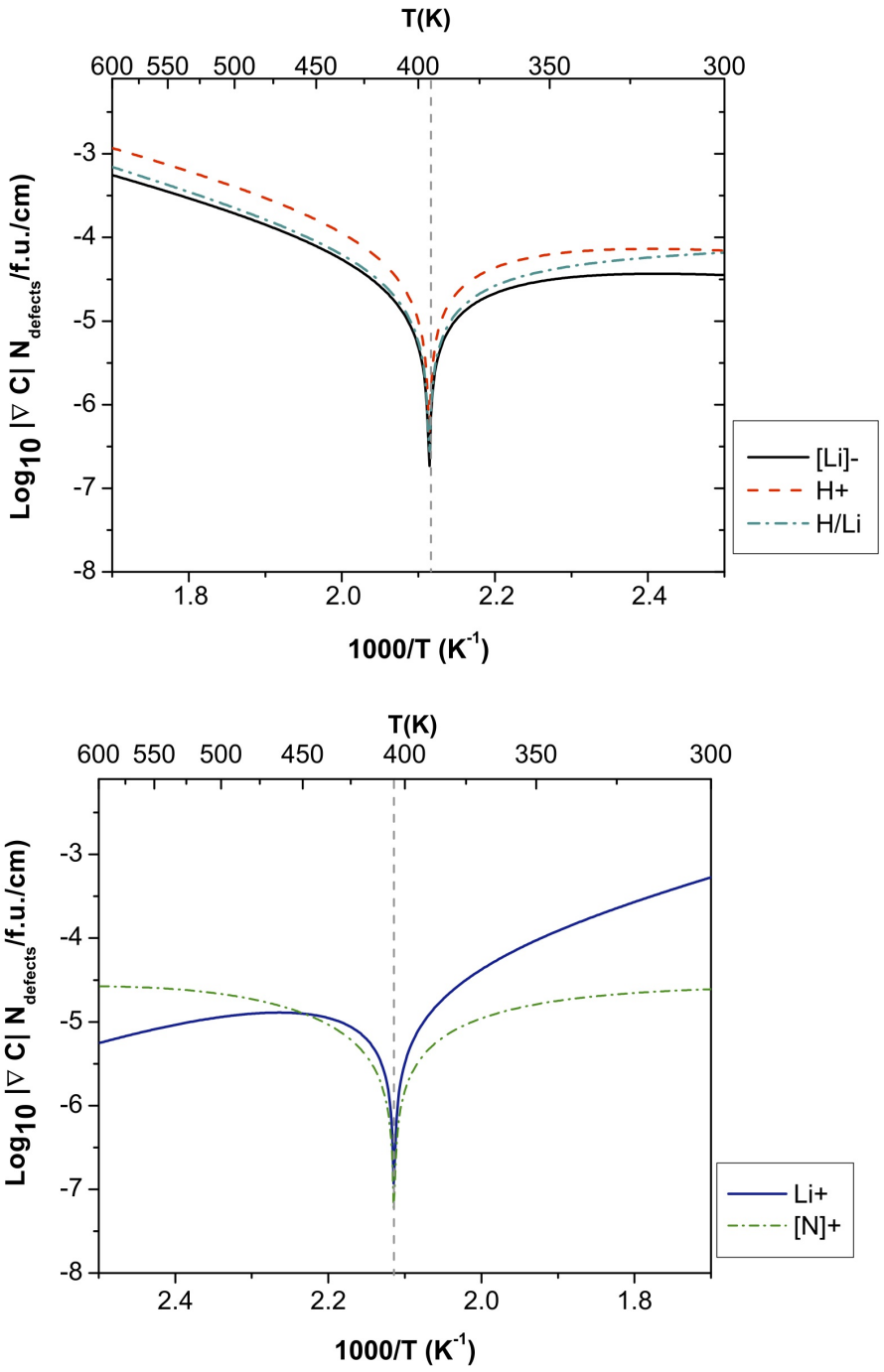

Figure 3.11: Concentration gradients in Li_2NH moving toward the LiH/Li_2NH interface (top) during dehydrogenation, and toward the Li_2NH/ $LiNH_2$ interface (bottom).

the $LiNH_2$ phase will be larger. Furthermore, the defects with the highest gradients are of the most interest in finding out the migration barrier. Finding the migration barrier is a computationally expensive task, so when screening for possible candidates for migration, the concentration gradient is a good primary litmus test. In the following section it will be explained how the migration barrier is obtained.

Table 3.2: The free energies and concentrations (number of defects per f.u.) of all defects in L_2iNH at 500K

Defects	$LiH : LiNH_2 : H_2$ [c]			$LiNH_2 : Li_2NH : H_2$ [d]		
	ΔH_{500K} [a]	ΔG_{500K} [a]	C_{500K} [b]	ΔH_{500K} [a]	ΔG_{500K} [a]	C_{500K} [b]
$[Li]^-$	0.286	0.329	9.57×10^{-4}	1.023	0.328	9.68×10^{-4}
$[H]^-$	1.070	0.525	4.03×10^{-5}	1.102	0.558	1.902×10^{-5}
${}^{i}Li^{+}_{tetra1}$	0.706	0.372	7.04×10^{-4}	-0.031	0.3729	6.971×10^{-4}
${}^{i}Li^{+}_{tetra2}$	0.845	0.601	3.48×10^{-6}	0.108	0.6017	3.448×10^{-6}
${}^{i}Li^{+}_{tetra3}$	0.713	0.423	2.14×10^{-4}	-0.024	0.4241	2.126×10^{-4}
${}^{i}Li^{+}_{octahedral}$	0.864	0.469	7.49×10^{-5}	0.127	0.4694	7.417×10^{-5}
${}^{i}H^{+}$	1.082	1.34	6.22×10^{-14}	1.115	1.372	2.931×10^{-14}
Li_H	1.201	0.2605	4.38×10^{-3}	0.497	0.297	2.044×10^{-3}
$[NH]^0$	0.237	0.177	3.21×10^{-2}	-0.467	0.210	1.51×10^{-2}
$[NH_2]^+$	1.083	0.764	1.97×10^{-8}	0.3457	0.765	1.944×10^{-8}

[a] in units of eV/Atom
[b] number of defects in f.u. per
[c] For the interface between solid state LiH / $LiNH_2$ and gaseous H_2
[d] For the interface between solid state $LiNH_2$ /Li_2NH and gaseous H_2

3.4.4 Migration Barrier

In order to obtain the full activation energies, migration barriers are needed for each defect of a low enough formation energy. First, in order to obtain the formation energy for dehydrogenation from Eq. 3.6, linear fits are taken at temperatures close to the critical temperature of the concentration gradient plots. This value is the exact formation energy, including all corrections to the energy via the temperature dependence, the periodic lattice.

Diffusion calculations in Li_2NH were done for the following defects, positively charged lithium interstitial ${}^{i}Li^{+}$, negatively charged lithium vacacancy $[Li]^{-}$, H^{+} interstitial and H^{-} vacancy. Interstital lithium in Li_2NH has two low-energy sites, an octahedral site relative to the N sublattice, and a tetrahedral site with a distance of 2.11 Åfor the jump. Diffusion of lithium vacancies is defined as a jump between two sites of the closest possible distance in the perfect Li_2NH structure. This corresponds to a distance of about 0.28 Å. The energy barrier for this jump is about 0.5 eV. The positively charged hydrogen interstitial diffuses in a manner similar to the neutral H_{Li} substitutional defect in Li_2NH. The bond distances to the two N ions are 1.4 Å, and 1.39 Å, i.e. they are equal within the computational accuracy. The energy barrier is 0.906 eV. Table 3.4 gives the activation barriers for defects moving in the Li_2NH phase are given. The defects that facilitate mass transport have the lowest formation energy and must be charge compensating in the bulk. In Li_2NH this can be achieved with the negatively charged Li interstitial, the negatively charged Li vacancy and the positively charged H interstitial. In this scenario $LiNH_2$ is dehydrated by H^{+} and $[Li]^{-}$ moving toward the lithium rich interface and the Li^{+} moving toward the LiH interface.

Table 3.3: Activation energy for mass transport in $LiNH_2$.

defect	ΔH^{mig}(kj/mol)	$\Delta H^{formation}$(kj/mol)	$E_{activation}$
[NH]	192	25	217
$[H]^-$	102	131	233
$[Li]^-$	–	107	–
Li^+	–	113	–

The competing kinetic pathway is diffusion through $LiNH_2$. The negatively charged hydrogen vacancy diffuses in Li_2NH through hydrogen dissociating from the H-N bond and forming a new H-N bond. At the transition state the distances to the two N ions are 1.49 Å, and 1.46 Å. The static energy barrier is calculated to be 1.8 eV, twice higher than the barrier for the interstitial H^+. This shows that the diffusion of this negative defect will be very slow. Also neutral [NH] vacancies are calculated, but found to have a migration barrier over 190 kJ/mol, and combined activation energy of over 200 kJ/mol. The migration barriers of the lithium species were not calculated. While their formation energies were low enough for a really small migration barrier to put them in the correct range for the experimental activation barrier, they failed the test of charge compensation. As can be seen from Figure 3.11 the two defects are moving in the opposite direction, however also opposite charge. This violates the net charge neutrality condition, and thus defects moving through $LiNH_2$ are not a competitive kinetic pathway. It is concluded that in the dehydrogenation of $LiNH_2$-LiH hydrogen interstitials and lithium species moving through the product phase, Li_2NH are the limiting process in this reaction.

Table 3.4: Activation energy for has transport in Li_2NH.

defect	ΔH^{mig}(kj/mol)	$\Delta H^{formation}$(kj/mol)	$E_{activation}$
H_{Li}	45	93	138
Li^-	55	31	86
$[Li]^-$	53	49	102
H^+	55	87	130

3.5 Discussion

The free energies, concentrations, concentration gradients and migration barriers of defects in two metal hydrides have been calculated. We find the following:

- Concentration gradients were obtained for the dehydrogenation of $LiNH_2$-LiH from which the formation energy can be extracted.
- Migration barriers were found in $LiNH_2$ and Li_2NH.
- Defects moving through the $LiNH_2$ phase have been shown to have much higher activation energies than have been found experimentally
- Mass transport through the Li_2NH phase is dominated by H^+, $[Li]^-$ and Li^- species, with an activation energy of 130 kJ/mol.
- Migration of hydrogen species, H^+, through the Li_2NH phase is the limiting process

Experimentally it was reported that the activation energy is about 128 – 138 kJ/mol. Our calculations suggest that the defects controlling the overall flux must overcome an activation barrier of 130 kJ/mol, which falls within the experimental range for the activation energy.

The study concludes that diffusion is in fact the limiting process in the decomposition of lithium amide and lithium hydride. More generally though the work presents a template for further work in compound metal hydrides. The treatment of kinetics in this work provides an avenue to understanding the limits in the kinetics of hydrogen storage in complex hydrides.

CHAPTER 4

Full decomposition of $LiAlH_4$ via a two-step reaction involving Li_3AlH_6

4.1 Introduction

The decomposition of lithium alanate occurs as a two-step reaction:

$$3LiAlH_4 \rightarrow Li_3AlH_6 + 2Al + 3H_2, \tag{4.1}$$

$$Li_3AlH_6 \rightarrow 2LiH + Al + 3/2\ H_2. \tag{4.2}$$

Lithium alanate, $LiAlH_4$ releases hydrogen by undergoing Reaction 4.1 in the temperature range 112–220 °C, which is initiated by endothermic melting. However there have also been reports of isothermal composition without melting [103]. The first decomposition releases 5.3 wt% H_2. The second reaction occurs in the range of 123–260 °C, releasing 2.6 wt% H_2.

Early studies by Wiench et al. [104] used nuclear magnetic resonance on decomposed $LiAlH_4$, and observed an alternate reaction path to the above mentioned two-step mechanism.

$$LiAlH_4 \rightarrow LiH + Al + \frac{3}{2}H_2, \tag{4.3}$$

Andreasen et al. [105] calculated an activation energy of 0.85 eV for the decomposition of solid $LiAlH_4$, from kinetic measurements under isothermal conditions. They also obtained an activation energy of 0.84 eV for the reaction in 4.1 in liquid state. A variety of metal additives as dopants have been applied in this system in an attempt to improve kinetics and lower activation energy. Ball milling has been shown to slightly improve kinetics [106,107] . A ball milled sample of $LiAlH_4$ catalyzed by $NiCl_2$ has been shown to reduce the onset decomposition temperature by 50 °C [108]. Likewise, $TiCl_3$ doped samples of $LiAlH_4$ lowers the decomposition temperature to 60-75 °C [109].

Most notably, it has been shown by Liu et al. that Ti-doped $LiAlH_4$ can reversibly store hydrogen, at 7% wt H_2 released at 80°C [110]. However, in spite of promising results of lowered dehydrogenation temperature [111], conflicting reports have been found in the literature regarding kinetics of decomposition. Activation energies for undoped and Ti-doped $LiAlH_4$ have shown only small differences within the experimental error. Andreassen [105] report an activation energy of 0.84eV for undoped and 0.92 eV for doped samples of $LiAlH_4$. Similarly Blanchard et. al [112] reported activation energies of 1.06 eV for undoped and 0.99 eV for samples doped with $TiCl_3/3AlCl_3$.

It remains unclear in what way doping affects the decomposition reaction 4.1, and a thorough study of the fundamental processes on a microscopic level could further improve our understanding of kinetic processes in metal hydrides.

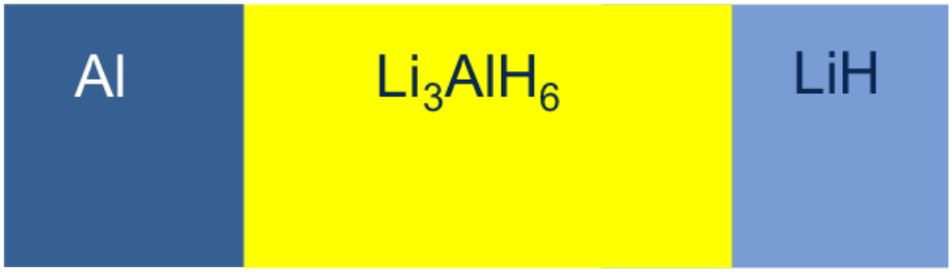

Figure 4.1: Morphology of mass transport through Li_3AlH_6.

4.2 Methods

4.2.1 Morphologies

A linearized version of the morphology with Li_3AlH_6 as the diffusive phase is given in Figure 4.1.

The defects are assumed to travel through the hexahydride, as it is known that creating lithium defects in aluminum is too high, so aluminum won't be the diffusive phase. Furthermore, results have shown that Al defects in LiH also have a very high formation energy [113]. Aluminum defects must be created in LiH, if it is the diffusive phase, since in the desorption of Li_3AlH_6 involves the transfer of aluminum species from the hexahydride to elemental aluminum formed in the products. Therefore it is concluded that the highest flux of native defects during the desorption of H_2 in Li_3AlH_6 happens in that phase.

4.2.2 Concentrations of Native Defects and Fermi levels

The equilibrium concentrations of all defects in the lithium tetrahydride and hexahydride phases were determined according to the equations discussed in chapter

3, Eqns. 3.7 and 3.8. The activation barrier is determined according to Eqn. 3.6. The electron chemical potential ϵ_F (i.e., the Fermi level) is referenced to the valence-band maximum (VBM), E_{VBM} of the bulk material. Concentration gradients, ∇C_i are calculated from differences in concentrations ΔC_i on each interface, divided by the distance between these interfaces, where d = 1 μm is set arbitrarily. And the Fermi level is used to determine charge neutrality. The rest of the methods of Chaper 3. are followed closely.

4.2.3 Chemical Potentials

The Chemical potentials are crucial at the interfaces based on Fig. 4.1. Only mass transport through Li_3AlH_6 is considered. The relevant coexisting phases are Li_3AlH_6, LiH, and H_2 at the right interface, and Li_3AlH_6, Al and H_2 at the left interface. The free energy equations at the interface between LiH and Li_3AlH_6 is given by:

$$\begin{aligned} G(Li_3AlH_6) &= 3\mu_{Li} + \mu_{Al} + 6\mu_H, \\ G(LiH) &= \mu_{Li} + \mu_H, \\ G(H_2) &= 2\mu_H, \end{aligned} \tag{4.4}$$

where $G(Li_3AlH_6)$ is the free energy of Li_3AlH_6 . Additionally, $G(H_2)$ includes the the gas phase hydrogen energy discussed in Section 2.2.1. At the left interface,

where Li_3AlH_6 is in contact with Al, the free energies are

$$\begin{aligned} G(Li_3AlH_6) &= 3\mu_{Li} + \mu_{Al} + 6\mu_H, \\ G(Al) &= \mu_{Al}, \\ G(H_2) &= 2\mu_H. \end{aligned} \tag{4.5}$$

The constraints of the chemical potentials at equilibrium, at each of the interfaces in the different morphologies result in chemical gradients between the interfaces. These chemical potential gradients result in fluxes that are essentially responsible for the phase separation of the dehydrogenation Reaction 4.2.

4.2.4 DFT Calculations

The calculations were carried out with density functional theory as implemented by the Vienna Ab Intio Simulation Package [53]. The electronic structure of the system was described using the exchange-correlation functional [96] with the projector augmented wave (PAW) [2] method with an energy cutoff of 875 eV. K-point sampling was performed for a 1x1x1 supercell of 480 atoms for the Li_3AlH_6 phase [or say the hexahydride phase] and a supercell of 384 atoms for the $LiAlH_4$ phase. Transition state calculations were performed using the Nudged Elastic Band method (NEB) [102].

4.3 Results for the decomposition of Li_3AlH_6

The assumption for mass transport is once again the migration of native defects. The equilibrium concentration of these defects are given by Equation 3.7.

4.3.1 Native Defect Energies and Concentrations in Li_3AlH_6

The enthalpies, free energies, and concentrations of defects created at each interface at 500K, are given in Table 4.1. The Free energy is derived from the entropy of gaseous H_2, as given by equation 2.46. In the table it is obvious that at the Al/ Li_3AlH_6 interface the defects with the lowest formation energies are the interstitial and vacancy, charged Li defects, as well as the positively charged H vacancy. However, not taking the free energy of hydrogen into account, the enthalpy of the neutral [LiH] vacancy begins to play a stronger role. Without the temperature dependence accounted for, the qualitative interpretation of the results changes. At the Li_3AlH_6/ LiH the defects with the lowest formation energy are also the positively charged H vacancy along with the Li interstitial and vacancy defects. At both interfaces, these are also the defects with the highest concentrations. In Li_3AlH_6 defects traveling from one interface to the other do not get outcompeted by other defects. However the Fermi levels are still different at the two interfaces, resulting in a high gradient, that provides the driving force behind the defect migration.

Table 4.1: The free energies and concentrations (number of defects per f.u.) of all defects in Li_3AlH_6 at 500 K

Defects	$LiH : LiNH_2 : H_2$ [c]			$LiNH_2 : Li_2NH : H_2$ [d]		
	ΔH_{500K} [a]	$\Delta G^{H_2}_{500K}$ [a]	C_{500K} [b]	ΔH_{500K} [a]	$\Delta G^{H_2}_{500K}$ [a]	C_{500K} [b]
$[Al]^{3-}$	2.357	2.357	1.745×10^{-24}	2.372	3.279	8.853×10^{-34}
$[AlH]^{2-}$	2.267	1.965	1.559×10^{-20}	2.129	2.734	2.756×10^{-28}
$[AlH_2]^{-}$	2.242	1.637	3.77×10^{-18}	1.952	2.344	1.907×10^{-23}
$[AlH_3]$	2.611	1.704	6.68×10^{-18}	2.167	2.167	1.432×10^{-22}
$[AlH_4]^{+}$	3.018	1.808	5.910×10^{-19}	2.421	2.119	4.414×10^{-22}
$[AlH_5]^{2+}$	3.516	2.005	6.195×10^{-21}	2.767	2.162	1.612×10^{-22}
$[AlH_6]^{3+}$	4.322	2.508	5.249×10^{-26}	3.419	2.512	4.757×10^{-26}
$[H]^{+}$	1.262	0.959	2.13×10^{-10}	1.109	0.806	7.425×10^{-9}
$[H]^{-}$	1.733	1.431	3.729×10^{-15}	1.887	1.584	1.071×10^{-16}
$^{i}H^{+}$	1.433	1.735	3.254×10^{-18}	1.278	1.582	1.133×10^{-16}
$^{i}H^{-}$	1.153	1.455	2.144×10^{-15}	1.306	1.608	6.155×10^{-17}
[LiH]	0.859	1.162	1.934×10^{-12}	1.008	1.008	6.923×10^{-11}
$[Li]^{-}$	0.086	0.690	1.099×10^{-7}	0.387	0.689	1.135×10^{-7}
$^{i}Li^{+}$	1.295	0.690	1.097×10^{-7}	0.99	0.692	1.061×10^{-7}

[a] in units of eV/atom
[b] number of defects in f.u. per
[c] For the interface between solid state Li_3AlH_6 / LiH and gaseous H_2
[d] For the interface between solid state Al / Li_3AlH_6 and gaseous H_2

The plots shown in Figure. 4.2, confirm that the temperature dependence for defects in the Li_3AlH_6 arises from the hydrogen. At the Li_3AlH_6/ LiH interface no discernible temperature dependence in the enthalpy is reported. The concentration plots in Figure 4.3, show concentration temperature dependencies of the defects with the lowest formation energy at the Al / Li_3AlH_6 interface (top panel) and the Li_3AlH_6/ LiH interface (bottom panel). The concentrations show Arrhenius behavior of all the defects. The defects that dominate the flux, or the ones that have the highest concentrations are interstitial and vacancy Li species, positively charged H vacancy and neutral [LiH] vacancy. At both interfaces the lithium species match each other's concentrations at each temperature. Without a third defect to balance out the charge, the combined lithium species would not contribute to the total flux. However the relatively high concentration of the positively charged H vacancy suggests that flux is dominated by the $[H]^+$ vacancy, and balanced out in charge by the Li species.

Finally the concentration gradients of the defects plotted in the concentration plots shows the defects with the highest gradients, and therefore those most likely to contribute to the competing process. At about 500 K a linear fit is taken from all the defects to calculate the formation enthalpy, as has been done in Chap. 3. The formation enthalpies are listed in Table 4.2. At about 275K the free energy goes to zero and no net mass flows through the diffusive phase. At low temperatures, Li_3AlH_6 is rehydrated, and Reaction 4.2 occurs in reverse. From this plot it is fairly obvious that the defect with the highest gradient is in fact positively charged H vacancy, balanced out by charged Li interstitials and vacancies.

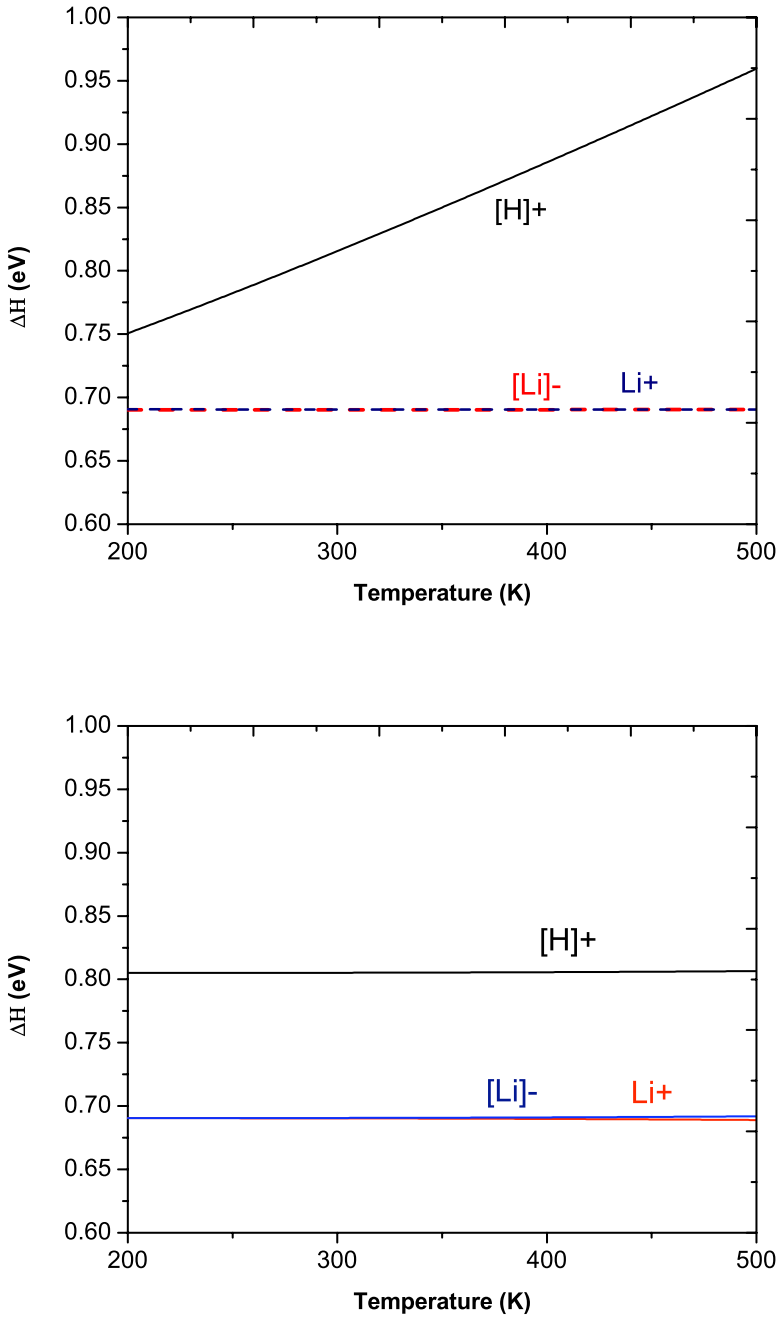

Figure 4.2: The free energies of defects in Li_3AlH_6 plotted against temperature, at Li_3AlH_6/Al interface (top) and Li_3AlH_6/ LiH interface (bottom).

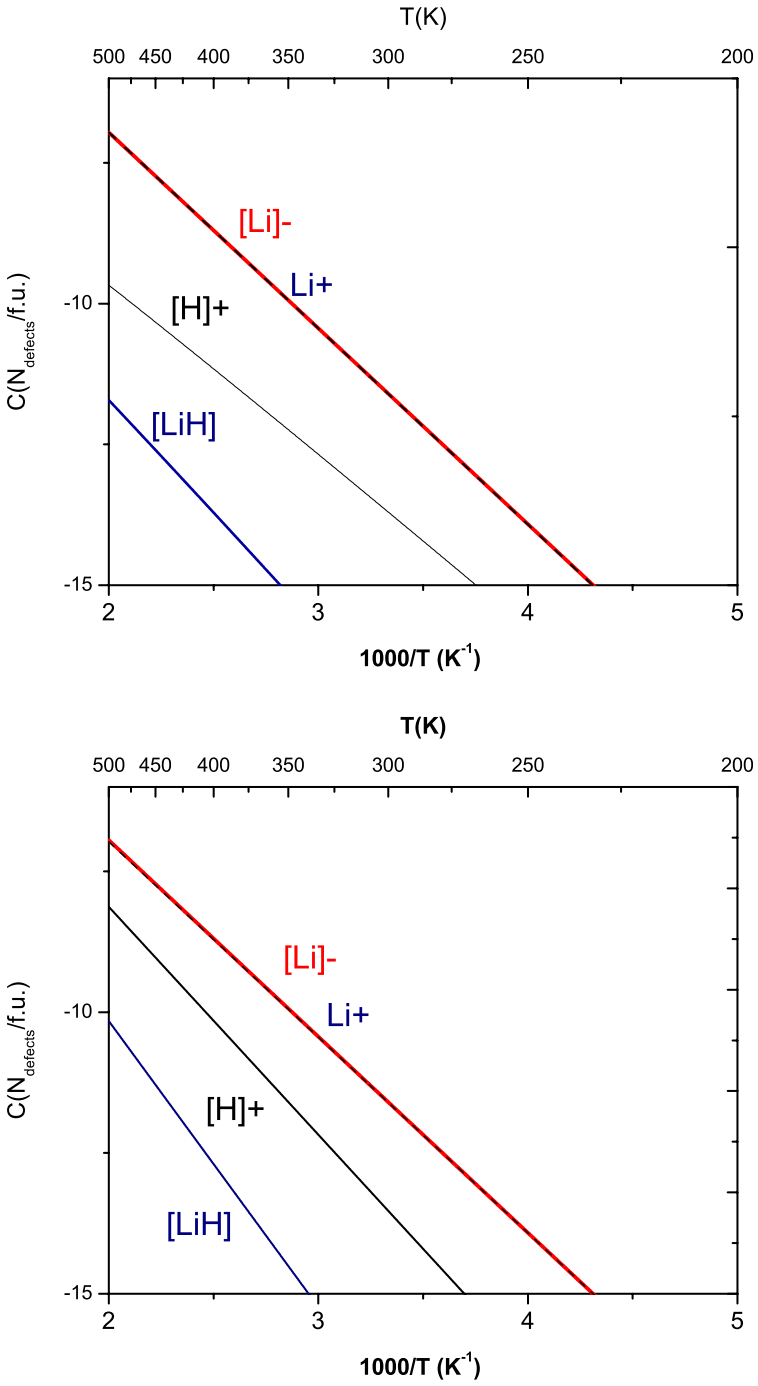

Figure 4.3: The concentrations of defects in Li_3AlH_6 plotted against temperature, at Li_3AlH_6 / Al interface (top) and Li_3AlH_6/ LiH interface (bottom).

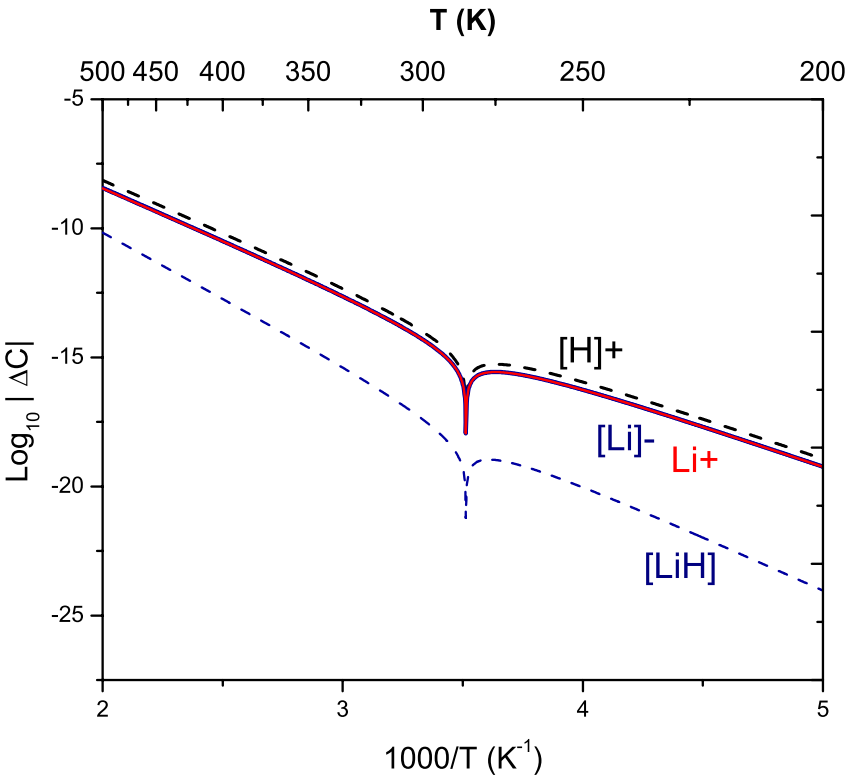

Figure 4.4: Highest defect concentration gradients vs. temperature in Li_3AlH_6.

4.3.2 Migration Barriers

4.3.3 Kickout mechanism of point defects in Li_3AlH_6

Bulk diffusion through a metal lattice generally occurs through one of two mechanisms, the conceptually simple mechanism of *direct diffusion*, or *indirect diffusion*. In direct diffusion, foreign atoms occupy empty sites, known as interstitial sites, in an otherwise perfect lattice, and migrate in discrete jumps from one interstitial site to another. On the other hand, *indirect diffusion* by definition involves intrinsic point defect in its mechanism [114–116]. Vacancies are merely voids created in the pure lattice, and atoms diffuse directly on the lattice, by exchanging places with vacancies. Bulk diffusion via vacancy migration is considered *indirect diffusion*. The vacancy mechanism is known to mediate self-diffusion in metals [117, 118], as well as metalloids, such as germanium, and silicon below 1270 K [114]. Furthermore it was determined by LeClaire in 1978, [119] that impurities in a lattice diffuse via the vacancy mechanism provided that their diffusion rates are comparable to the self-diffusion rate of the host. Otherwise, the vacancy mechanism is not possible, and another mechanism for diffusion controls bulk migration. It is suggested to be an interstitial type of mechanism, which in the case of *indirect diffusion* is referred to as the kick-out mechanism. When foreign atoms (A) are incorporated in the lattice under the conditions of thermal equilibrium, they enter either as substitutional atoms, A_s or interstitial A_i. Then they would diffuse either by a dissociative mechanism, or a kick-out mechanism. The mobility of foreign atoms is higher when they are positioned in the interstices, than when they are on regular lattice sites. The two mechanisms are distinguished by the way they interchange

foreign atoms between substitutional atom and interstitial atom configurations.

The dissociative mechanism involves transitions between A_s, substitutional atoms, and A_i interstitial atoms via a vacancy, V:

$$A_s \rightleftharpoons A_i + V. \tag{4.6}$$

The forward direction of Equation 4.6 can be seen as the dissociation of a substitutional foreign atom A_s into a Frenkel pair with an interstitial partner A_i, and the backward into a recombination of a vacancy and an interstitial into a substitutional foreign atom.

The kick-out mechanism involves self-interstitials, as in Equation 4.7:

$$A_s + I \rightleftharpoons A_i. \tag{4.7}$$

In the forward direction, an interstitial host atom and foreign atom substituted on a lattice site exchange relative positions, creating an interstitial foreign atom A_i. In the backward direction an interstitial foreign atom A_i displaces a lattice atom into an interstitial site, or "kicks it out" of its lattice site. To complete the jump, another step is required in which the foreign atom hops to the nearest interstitial site, or in other words another forward reaction of Eq. 4.7. In this manner, the interstitial foreign atom A_i hops on interstitial sites by kicking the host atoms out of lattice sites as intermediate steps.

It's worth noting that Reactions 4.6 and 4.7 are not symmetric in their exchange of interstitial atom and vacancy, and can have vastly different theoretical prediction. The kick-out method has been observed in the diffusion of foreign elemental

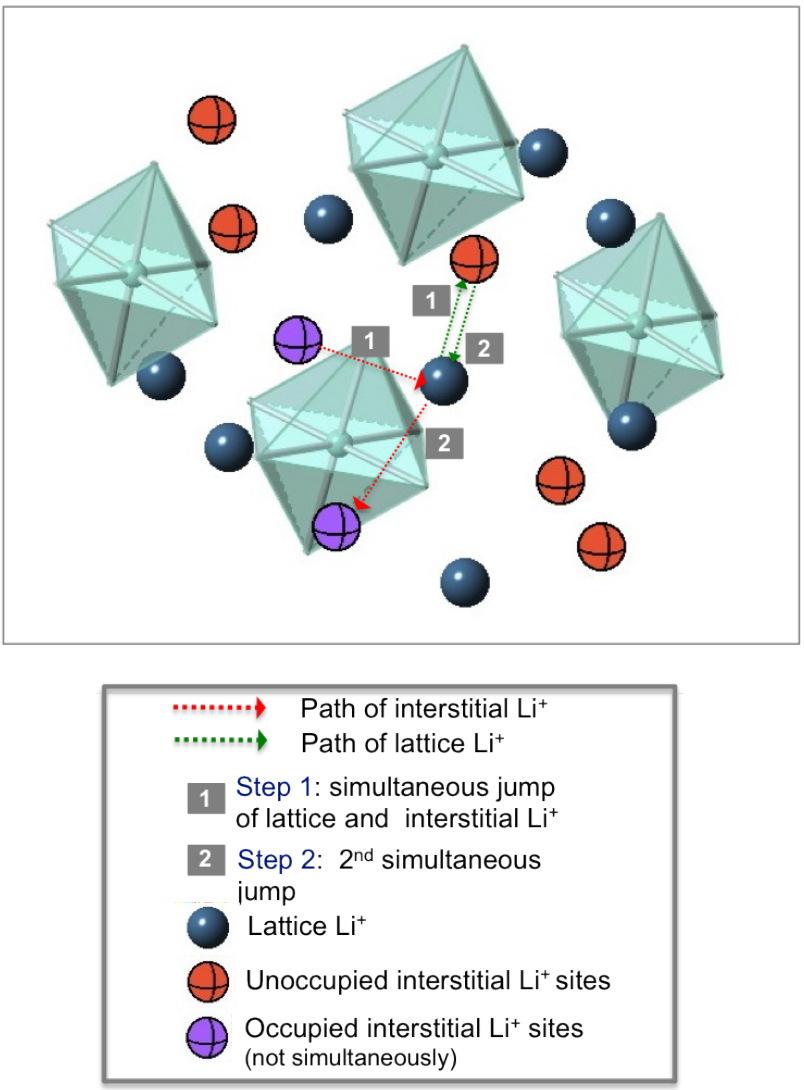

Figure 4.5: The kick out mechanism in Li_3AlH_6; illustrated as a series of two separate steps.

semiconductors [103, 115, 120], as well as the key step to self-diffusion of Si [115]. However it has so far not been identified as a mechanism of defect migration for ordered alloys. In this work, it has been found to be the mechanism for the diffusion of lithium interstitial species in the hexahydride phase, Li_3AlH_6. An illustration of the mechanism can be seen in Figure 4.5. The blue atoms are the original lithium lattice sites. The orange atoms have been determined to be interstitial sites for lithium atoms. These sites were determined by symmetry operations on the lattice. First a mesh of lithium atoms has been layer over the Li_3AlH_6 lattice with a width of 0.5 Å, taking into account ionic radii of the present atoms (the lithium atoms and the AlH_6 clusters). The remaining atoms on the mesh were relaxed using DFT and the relaxed positions are considered the interstitial sites. In Figure 4.5, the purple atoms denote two interstitial sites between which a diffusion event occurs, hence they are not both occupied with Li atoms at the same time. The distance between the two atoms is 2.3 Å. It was first assumed that the interstitial would travel from one purple site to the other directly. However it was found that instead, the event occurs in two separate steps. During *step one*, the interstitial Li^+ at the occupied purple site moves to the blue lattice site while simultaneously the (kicked-out) lattice Li^+ (at that site) hops to an adjacent unoccupied lithium (pictured in orange). During *step two* the interstitial Li^+ returns from the lattice site (in blue) to another interstitial site (second purple) and the lattice Li^+ returns to its original site, from the adjacent interstitial (orange) site. In Figure 4.5 the distinct paths of the interstitial Li^+ and lattice Li^+ are denoted by red, and green arrows respectively. The steps that occur at the same time are also numbered, in little grey boxes. The two separate steps have different activation barriers. *Step one* has a calculated barrier of 0.38 eV/atom, and *Step two* has a barrier of 0.45

eV/atom. Since both steps are necessary for mass transport, the higher of the two paths is considered as the overall migration barrier for the diffusion of interstitial Li^+ species in Li_3AlH_6. The results are summarized in Table 4.2

4.3.4 Activation Energies for defects in Li_3AlH_6

A summary of activation energies is given by Table 4.2. The other migration barriers, for the $[Li]^-$ and the $[H]^+$ have been obtained in a fairly straightforward way using the NEB method. In order to account for charge compensation, the lowest energy defect, negatively charged Li vacancy can be balanced with the positively charged H vacancy, both moving toward the Al / Li_3AlH_6 interface. The higher of the two energies is the limiting process. According to the calculations presented here, the limiting process for the desorption of Li_3AlH_6 is the diffusion of positively charged H vacancy moving the Li_3AlH_6/ Al interface, with an activation energy of 124 kJ/mol. However, experimentally the activation barrier has been found to be between 92-100 kJ/mol. It should be noted that vibrational contributions to the energy are not included. Likewise tunneling effects, and the prefactor to the Arrhenius equation was not considered. By including all those corrections, it would be possible to obtain a more conclusive answer. In this work, it is clear that diffusion cannot be excluded as a possible limiting process to reaction kinetics.

4.4 Results for the decomposition of $LiAlH_4$

Now the first decomposition Reaction, 4.1 is considered. This reaction is exothermic, and has so far not been consistently destabilized using metal species. The

Table 4.2: Activation Energy for the final defects formed in Li_3AlH_6

defect	$\Delta H^{formation}$(kj/mol)	ΔH^{mig} (kj/mol)	$E_{activation}$
Li^+path1	81	37	
Li^+path2	81	$45^{*barrier}$	126
$[Li]^-$	81	30	111
[H]+	81	43	124

Figure 4.6: Morphology of mass transport through $LiAlH_4$.

morphology for the case of defects moving through the diffusive phase $LiAlH_4$ is given in Figure 4.6.

It should be noted that the concentration gradient calculations performed to obtain the formation energies were also calculated in the case of Li_3AlH_6 as the diffusive phase in Reaction 4.1. However it was found that for the defects with low enough formation energies to qualify as the dominant flux, it was found that the migration barriers are higher than in $LiAlH_4$. Therefore Li_3AlH_6 has been ruled out as the diffusive phase in the desorption of $LiAlH_4$.

4.4.1 Chemical Potentials

The chemical potentials at the interfaces based on Fig. 4.6 are listed. The coexisting phases are Li_3AlH_6, $LiAlH_4$, and H_2 at the left interface, and $LiAlH_4$, Al and

H_2 at the right interface. The free energy equations at the interface between LiH and Li_3AlH_6 are given by:

$$\begin{aligned} G(Li_3AlH_6) &= 3\mu_{Li} + \mu_{Al} + 6\mu_H, \\ G(LiAlH_4) &= \mu_{Li} + \mu_{Al} + 4\mu_H, \\ G(H_2) &= 2\mu_H, \end{aligned} \tag{4.8}$$

where $G(LiAlH_4)$ is the free energy of $LiAlH_4$. Additionally, $G(H_2)$ includes the the gas phase hydrogen energy discussed in Section 2.2.1. At the right interface, where $LiAlH_4$ is in contact with Al, the free energies are

$$\begin{aligned} G(LiAlH_4) &= \mu_{Li} + \mu_{Al} + 4\mu_H, \\ G(Al) &= \mu_{Al}, \\ G(H_2) &= 2\mu_H. \end{aligned} \tag{4.9}$$

The constraints of the chemical potentials at equilibrium at each of the interfaces in the different morphologies result in chemical gradients between the interfaces. These chemical potential gradients result in fluxes that are essentially responsible for the phase separation of the dehydrogenation Reaction 4.1.

4.4.2 Native Defect Energies and Concentrations in $LiAlH_4$

Enthalpies, free energies and concentrations for defects in $LiAlH_4$ at 500 K, formed at the $LiAlH_4$ / Li_3AlH_6, and the $LiAlH_4$ / Al interfaces are given in Table 4.3. At this temperature, where dehydrogenation of $LiAlH_4$ occurs, the lowest free

formation energy at the $LiAlH_4$ / Li_3AlH_6 interface is for the Li defects, both interstitial and vacancies. Other low formation energies are for the $[AlH_4]^+$ defect, one of the positively charged H sites, and the interstitials, negatively charged H defect. These are also the defects that have the highest concentrations at this interface. At the Li_3AlH_6/ LiH the defects with the lowest free energies, and consequently highest concentrations, are now the positively charged Li interstitials, and the negatively charged H interstitials and vacancies. The free energy for the $[AlH_4]^+$ defect is still low. Additionally, this analysis changes qualitatively when the gas phase free energy correction is not accounted for.

Table 4.3: The free energies and concentrations (number of defects per f.u.) of all defects in $LiAlH_4$ at 500 K

Defects	$LiH : LiNH_2 : H_2$ [c]			$LiNH_2 : Li_2NH : H_2$ [d]		
	ΔH_{500K} [a]	$\Delta G^{H_2}_{500K}$ [a]	C_{500K} [b]	ΔH_{500K} [a]	$\Delta G^{H_2}_{500K}$ [a]	C_{500K} [b]
$[Al]^{3-}$	1.967	2.873	1.08×10^{-29}	0.487	0.487	1.241×10^{-5}
$[AlH]^{2-}$	1.834	2.439	1.595×10^{-25}	0.879	0.576	1.555×10^{-6}
$[AlH_2]^{-}$	1.855	2.158	1.785×10^{-22}	1.423	0.818	5.589×10^{-9}
$[AlH_3]$	1.552	1.552	2.25×10^{-16}	1.644	0.738	3.681×10^{-8}
$[AlH_4]^{+}$	1.008	0.705	7.765×10^{-8}	1.623	0.414	6.637×10^{-5}
$[H]^{+}_{site1}$	1.158	0.856	2.355×10^{-9}	1.682	1.38	1.231×10^{-14}
$[H]^{+}_{site2}$	0.939	0.637	3.791×10^{-7}	1.463	1.161	1.981×10^{-12}
$[H]^{-}$	1.183	0.880	1.335×10^{-9}	0.659	0.356	2.55×10^{-4}
${}^{i}H^{+}$	0.953	1.255	2.205×10^{-13}	1.477	1.780	1.151×10^{-18}
${}^{i}H^{-}_{site1}$	0.526	0.828	4.449×10^{-9}	0.002	0.305	8.508×10^{-4}
${}^{i}H^{-}_{site2}$	0.472	0.775	1.558×10^{-8}	-0.051	0.251	2.972×10^{-3}
[LiH]	0.875	0.875	1.514×10^{-9}	0.783	1.690	9.257×10^{-18}
$[Li]^{-}$	0.222	0.524	5.199×10^{-6}	-0.394	0.815	6.083×10^{-9}
${}^{i}Li^{+}$	0.830	0.528	4.761×10^{-6}	1.446	0.237	4.053×10^{-3}

[a] in units of eV/atom
[b] number of defects in f.u. per
[c] For the interface between solid state $LiAlH_4$ / Al and gaseous H_2
[d] For the interface between solid state $LiAlH_4$ / Li_3AlH_6 and gaseous H_2

The free energy plotted with its temperature dependence is shown in Figure 4.7. At the Li_3AlH_6 /$LiAlH_4$ interface little change in behavior is observed with increasing temperature. The free energies stay about the same, with the exception of Li defects at high temperatures. However at the $LiAlH_4$ / Al interface there is non-Arrhenius behavior arising from some of the defects, which starting at about 230 K begin to show non linear curves. The charge setting defect at the first interface is the lithium interstitial/vacancy Frenkel pair. This non-Arrhenius behavior becomes obvious in Figure 4.8. At the second interface, at low temperatures, the Fermi level setting defects are the lithium species. However after about 350 C this happens with the interstitial lithium and the negatively charged hydrogen species. At the first interface the behavior is linear and obeys the Arrhenius relation. The charge neutrality is set by the lithium species. Finally in Figure 4.9 the gradients are given, based on defects that are moving in the same direction during dehydrogenation and rehydrogenation. The nonlinearity in the gradient at high temperatures comes from the non-Arrhenius behavior of defect concentrations. The $[AlH_4]^+$, the Li and H interstitials are moving toward the lithium-rich phase, or the Li_3AlH_6 /$LiAlH_4$ interface during dehydrogenation, and towards the aluminum interface during dehydrogenation. The Li and H vacancies move in the opposite direction. A linear fit is taken at high temperatures to determine the formation enthalpies that include all corrections. These are listed in Table 4.4, along with the migration barriers.

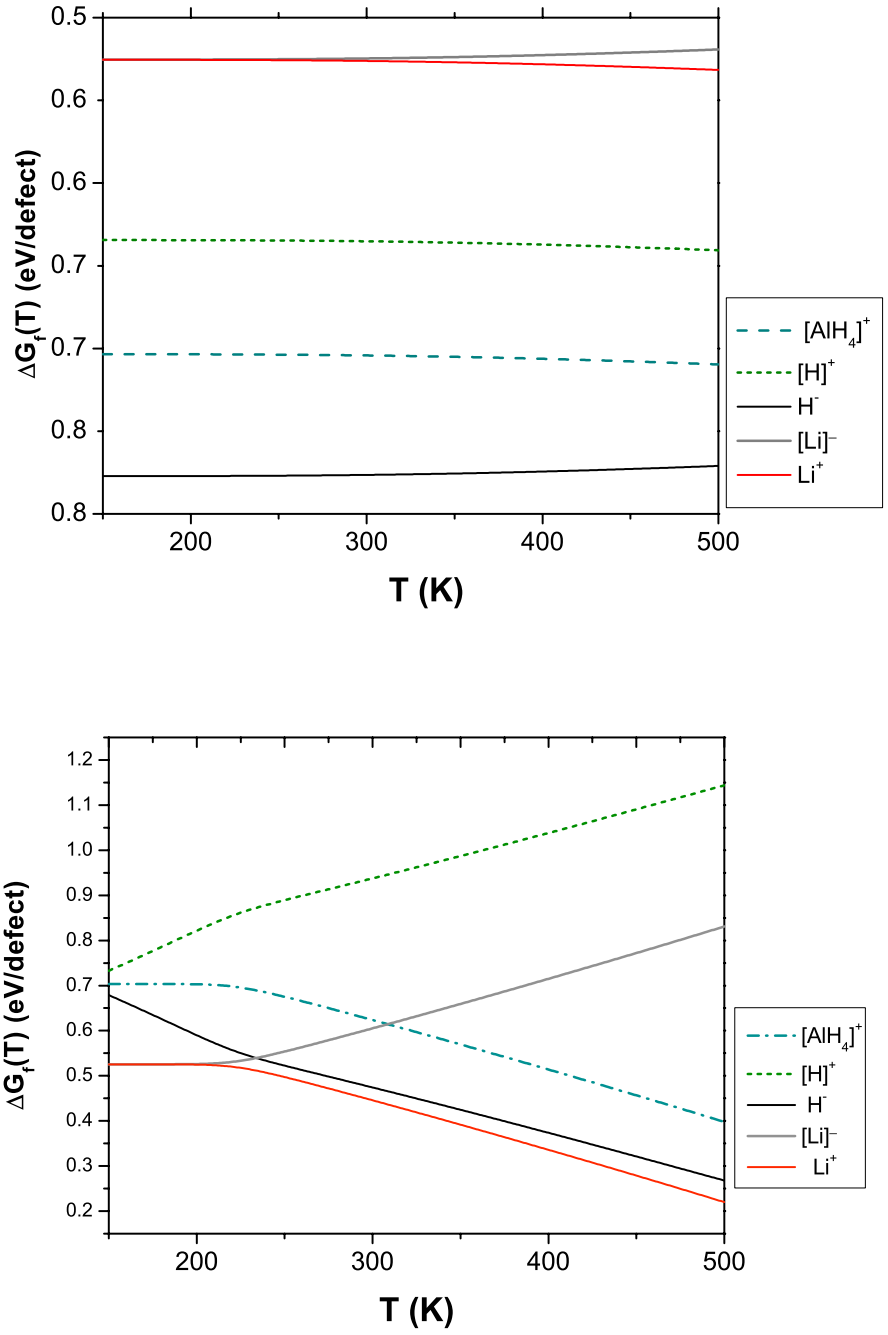

Figure 4.7: The free energies of defects in $LiAlH_4$ plotted against temperature, at $LiAlH_4$ / Li_3AlH_6 interface (top) and $LiAlH_4$ / Al interface (bottom).

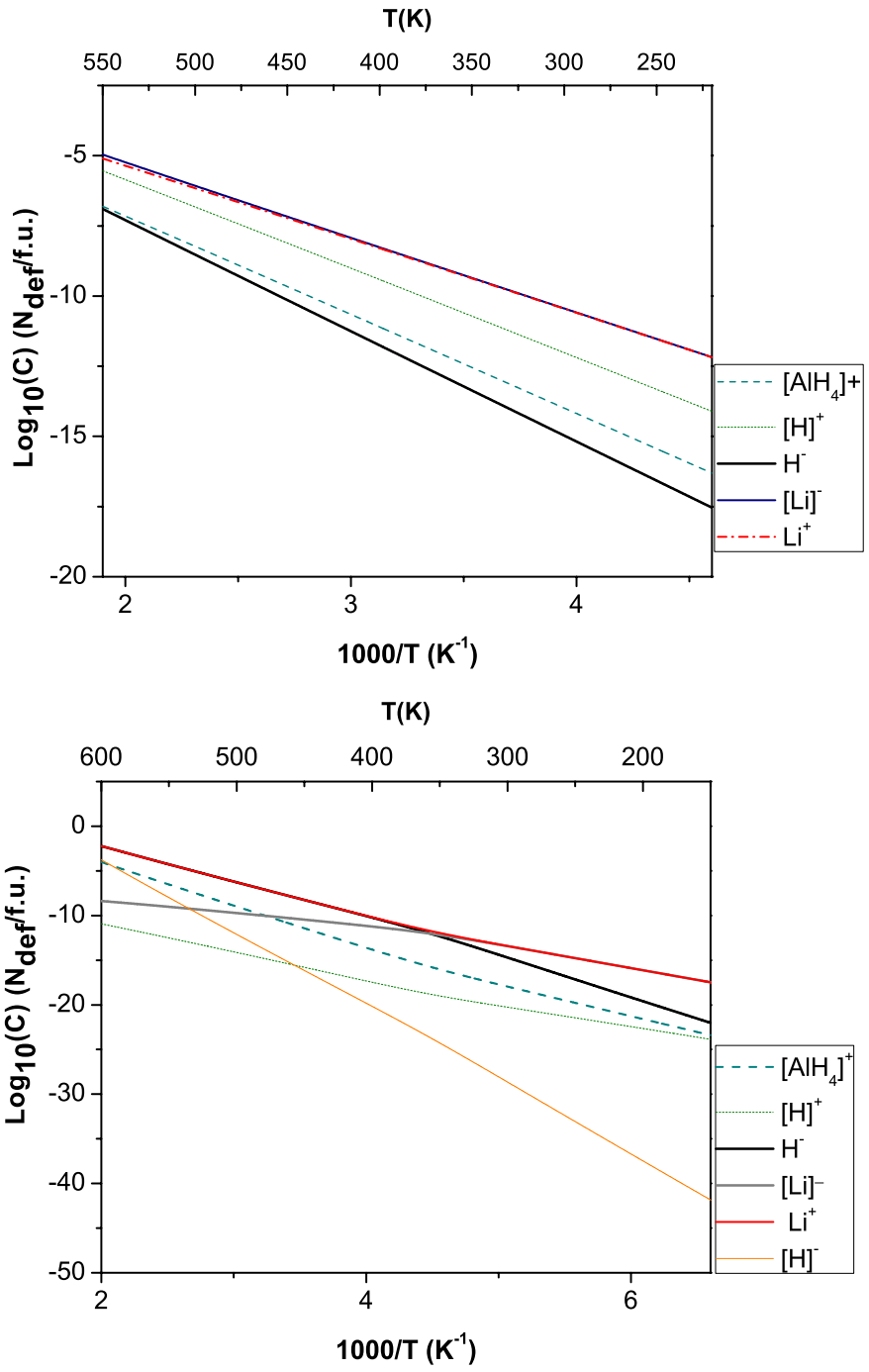

Figure 4.8: Concentrations of defects in $LiAlH_4$ plotted against temperature, at $LiAlH_4$ / Li_3AlH_6 interface (top) and $LiAlH_4$ / Al interface (bottom).

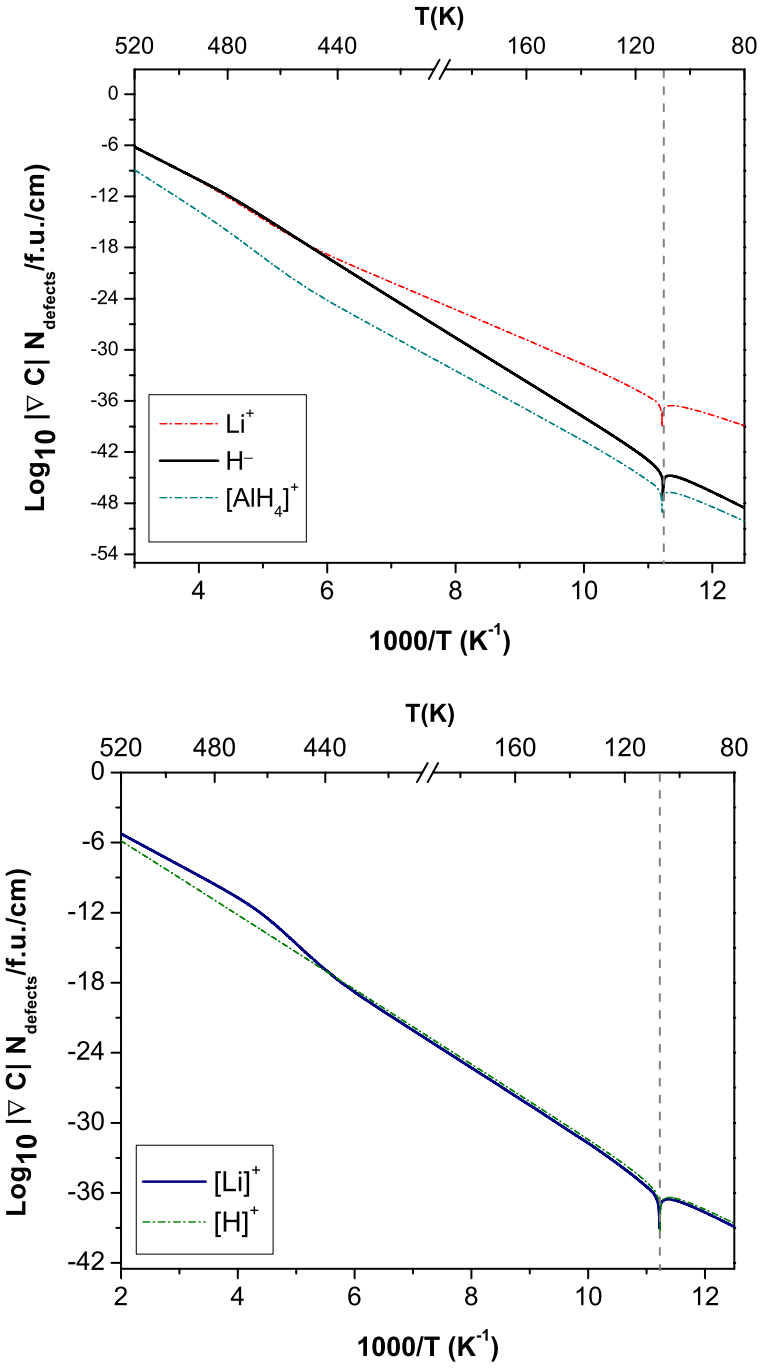

Figure 4.9: Concentration gradients of defects in $LiALH_4$ plotted against temperature, at $LiAlH_4$ / Li_3AlH_6 interface (top) and $LiAlH_4$ / Al interface (bottom).

Table 4.4: Activation energy for the final defects in $LiAlH_4$

defect	$\Delta H^{formation}$(eV/atom)	ΔH^{mig}(eV/atom)	$E_{activation}$
$[AlH_4]^+$	1.00	1.01	2.01
[H]+	0.62	0.30	0.92
H^+	0.50	0.63	1.20
H^-	0.79	0.30	1.04
$[Li]^-$	0.53	0.23	0.76
Li^+	0.81	0.22	1.00

4.4.3 Activation Energies for defects in $LiAlH_4$

The total activation energies for defects moving in the $LiAlH_4$ phase are given in Table 4.4. The formation enthalpies were linearly fitted from the concentration gradient plots in a temperature range of 450–550 K. In that temperature range, defects that are moving toward the Li_3AlH_6 /$LiAlH_4$ interface are interstitial Li^+ and interstitial H^-. On the other hand, negatively charged Li vacancy, positively charged hydrogen vacancy and interstitial H^+ are moving toward the $LiAlH_4$ / Al interface. In order to satisfy the condition of net charge neutrality, the defect with the lowest activation energy $[Li]^-$ must be properly balanced. Both $[H]^+$ and interstitial H^+ qualify for this criteria, they are of opposite charge, but moving toward the same interface. Of the three defects controlling the overall flux, the positively charged $[H]^+$ vacancy paired with the negatively charged $[Li]^-$ vacancy have the lowest activation energy, which is still in the range of the experimental value of 0.73 -1.06 eV/atom. Therefore it is concluded that the limiting process in the dehydrogenation of $LiAlH_4$ is the diffusion of positively charged, H vacancies.

4.5 Discussion

To determine the limiting process in the full desorption of lithium alanate, the free energies, concentrations, concentration gradients and migration barriers of the defects in $LiAlH_4$ and Li_3AlH_6 have been presented.

- Concentration gradients were obtained for the dehydrogenation of $LiAlH_4$ and Li_3AlH_6 from which the formation energies were extracted.
- Migration barriers were found in $LiAlH_4$ and Li_3AlH_6.
- A mechanism of diffusion, the kick-out diffusion mechanism, previously reported as only ocurring in elemental semiconductors, has been discovered in the Li_3AlH_6 metal hydride.
- Diffusion cannot be ruled out as the limiting process for the desorption of Li_3AlH_6.
- Mass transport through the $LiAlH_4$ phase is dominated by $[H]^+$, $[Li]^-$ and Li^+ species
- Li_3AlH_6 has been ruled out as the diffusive phase in the desorption of $LiAlH_4$.
- Migration of hydrogen species, $[H]^+$, through the $LiAlH_4$ phase is the limiting process

It should be noted that for the complete understanding of the underlying mechanisms for decomposition of lithium hexahydride, a thorough study of the vibrational contributions to the free energy is required. Though it is computationally

very expensive for a lattice of low symmetry to calculate the harmonic vibrational modes, it is evident from the work presented here that calculating only DFT energies is not always sufficient to reach a final conclusion about the fluxes controlling mass transport. The variational corrections to the total energies are in many cases substantial [100]. Further work on this system would clarify the unanswered questions regarding the limiting processes.

Regarding the mass transport in $LiAlH_4$, it is interesting to note that work on a similar hydride has been done elsewhere [92, 93], where it was concluded that in the desorption of Ti-catalyzed $NaAlH_4$ the limiting process is the flux of Na vacancies through the Na_3AlH_6 phase. The apparent lack of symmetry in diffusion mechanisms between these two metal hydrides at a cursory glance, could be attributed to size difference in the cations. Additionally the difference can be attributed to the nature with which the metal hydrides are desorbed. Extensive research has been done on $NaAlH_4$ to glean the mechanism by which Ti-doping influences both the lowering of the E_{act} and the reversibility of the reaction. It has however been concluded by Michel et al. [92] that the predicted Fermi level lowering in $NaAlH_4$ associated with Ti-doping is too small to account for the drop in the experimentally observed E_{act} associated with Ti-doping. Not only is it still unclear how doping affects sodium alanate, it also remains unclear, in spite of various experiments, how doping affects lithium alanate. The experiments, as noted in the introduction of this section, are not in agreement, and even the reversibility and exact activation energy of $LiAlH_4$ are still in question. Provided an experimental resolution as to how doping of $LiAlH_4$ affects kinetics, it would be valuable to expand upon this study by including dilute levels of dopant.

References

[1] P. B. Weisz. "Basic Choices and Constraints on Long-Term Energy Supplies,". *Physics Today*, 57:47–52, **2004**.

[2] Annual energy outlook 2014 with projections to 2040. *tech report*, **2014**.

[3] "Technically Recoverable Shale Oil and Shale Gas Resources: An Assessment of 137 Shale Formations in 41 Countries Outside the United States,". *Tech report*, **2013**.

[4] World energy resources survey. Technical report, World Energy Council, **2013**.

[5] "Department of Energy: Basic research need for electrical storage,". *tech report*, **2007**.

[6] M. Winter and J. R. Brodd. "What Are Batteries, Fuel Cells, and Supercapacitors?,". *Chemical Reviews*, 104(10):4245–4270, **2004**.

[7] H.N. Gupta. *Fundamentals of Internal Combustion engines*. PHI Learning Pvt. Ltd., **2006**.

[8] S. Litster and G. McLean. "PEM fuel cell electrodes,"'. *Journal of Power Sources*, 130:61 – 76, **2004**.

[9] "High strength Carbon Fibers- 2012 annual progress report,". Technical report, **2012**.

[10] Department of energy annual progress report. **2010**.

[11] O. M. Yaghi, M. O'Keeffe, N. W. Ockwig, H. K. Chae, M. Eddaouddi, and J. Kim. "Reticular synthesis and the design of new materials,". *Nature*, 423:705–14, **2003**.

[12] B. Panella and M. Hirscher. "Hydrogen Physisorption in Metal–Organic Porous Crystals,". *Advanced Materials*, 17(5):538–541, **2005**.

[13] H. K. Chae, D. Siberio-Perez, J. Kim, M. Eddaouddi, A. J. Matzger., M. O'Keeffe, and O. M. Yaghi. "A route to high surface area, porosity and inclusion of large molecules in crystals,". *Nature*, 427(523-7), **2004**.

[14] S. Satyapal, J. Petrovic, C. Read, G. Thomas, and G. Ordaz. "The U.S. Department of Energy's National Hydrogen Storage Project: Progress towards meeting hydrogen-powered vehicle requirements,". *Catalysis Today*, 120(3–4):246 – 256, **2007**. Proceedings of the Korea Conference on Innovative Science and Technology (KCIST-2005):Frontiers in Hydrogen Storage Materials and Technology.

[15] Z. Xiong, G. Wu, J. Hu, and P. Chen. "Ternary Imides for Hydrogen Storage,". *Advanced Materials*, 16(17):1522–1525, **2004**.

[16] E. C.E. Rönnebro and E. H. Majzoub. "Recent advances in metal hydrides for clean energy applications". *MRS Bulletin*, 38:452–458, 6 **2013**.

[17] L. Schlapbach. *Hydrogen in Intermetallic Compounds I. Electronic, Thermodynamic, and Crystallographic Propertie*. Springer-Verlag, **1988**.

[18] S. Orimo, Y. Nakamori, J. R. Eliseo, A. Züttel, and C. M. Jensen. "Complex Hydrides for Hydrogen Storage,". *Chemical Reviews*, 107(10):4111–4132, **2007**.

[19] D.R. Lide. *CRC Handbook or Chemistry and Physics.* New York:CDC Press, 83 edition, **2002**.

[20] J. B. Yang, X. D. Zhou, Q. Cai, W. J. James, and W. B. Yelon. "Crystal and electronic structures of $LiNH_2$,". *Applied Physics Letters*, 88(4):–, **2006**.

[21] H. Leng, T. Ichikawa, and H. Fujii. "Hydrogen Storage Properties of LiMgNH Systems with Different Ratios of $LiH/Mg(NH_2)_2$,". *The Journal of Physical Chemistry B*, 110(26):12964–12968, **2006**. PMID: 16805600.

[22] A. R. Akbarzadeh, V. Ozolins, and C. Wolverton. "First-Principles Determination of Multicomponent Hydride Phase Diagrams: Application to the Li-Mg-N-H System,". *Adv. Mater*, **2007**.

[23] A. R. Akbarzadeh, V. Ozolins, and C. Wolverton. "First-principles determination of crystal structures, phase stability, and reaction thermodynamics in the Li-Mg-Al-H hydrogen storage system,". *Adv. Mater*, 19:3233–9, **2008**.

[24] B. Bogdanović, R. A. Brand, A. Marjanović, M. Schwickardi, and J. Tölle. "Metal-doped sodium aluminium hydrides as potential new hydrogen storage materials,". *Journal of Alloys and Compounds*, 302(1–2):36 – 58, **2000**.

[25] J.J. Reilly and R.H. Wiswall. "Reaction of hydrogen with alloys of magnesium and copper,". *Inorg. Chem*, 6:2200, **1967**.

[26] J.J. Reilly and R.H. Wiswall. "Reaction of hydrogen with alloys of magnesium and nickel and the formation of Mg_2NiH_4",. *Inorg. Chem*, 7:2254, **1968**.

[27] J. Wang, H. Li, and P. Chen. "Amides and borohydrides for high-capacity solid-state hydrogen storage—materials design and kinetic improvements,". *MRS Bulletin*, 38:480–487, 6 **2013**.

[28] W. Luo. "(LiNH2–MgH2): a viable hydrogen storage system,". *Journal of Alloys and Compounds*, 381(1–2):284 – 287, **2004**.

[29] F. E. Pinkerton, M. S. Meyer, G. P. Meisner, and M. P. Balogh. "Improved hydrogen release from $LiB_0.33N_0.67H_2.67$ with metal additives: Ni, Fe, and Zn,". *Journal of Alloys and Compounds*, 433(1–2):282 – 291, **2007**.

[30] F. E. Pinkerton, G. P. Meisner, M. S. Meyer, and M.P. Baloghand M.D. Kundrat. "Hydrogen Desorption Exceeding Ten Weight Percent from the New Quaternary Hydride $Li_3BN_2H_8$,". *The Journal of Physical Chemistry B*, 109(1):6–8, textbf2005.

[31] G. P. Meisner, M. L. Scullin, M. P. Balogh, F. E. Pinkerton, and M. S. Meyer. "Hydrogen Release from Mixtures of Lithium Borohydride and Lithium Amide: A Phase Diagram Study,". *The Journal of Physical Chemistry B*, 110(9):4186–4192, **2006**. PMID: 16509713.

[32] Y. E. Filinchuk, K. Yvon, G. P. Meisner, F. E. Pinkerton, and M.P Balogh. "On the Composition and Crystal Structure of the New Quaternary Hydride Phase $Li_4BN_3H_10$,". *Inorganic Chemistry*, 45(4):1433–1435, **2006**.

[33] J. J. Vajo, S. L. Skeith, and F. Mertens. "Reversible Storage of Hydrogen in Destabilized LiBH4,". *The Journal of Physical Chemistry B*, 109(9):3719–3722, **2005**.

[34] S. V. Alapati., J. K. Johnson, and D. S. Sholl. "Identification of Destabilized Metal Hydrides for Hydrogen Storage Using First Principles Calculations,". *The Journal of Physical Chemistry B*, 110(17):8769–8776, **2006**.

[35] S. V. Alapati, J. J. Karl, and D. S. Sholl. "Using first principles calculations to identify new destabilized metal hydride reactions for reversible hydrogen storage,". *Phys. Chem. Chem. Phys.*, 9:1438–1452, **2007**.

[36] S. V. Alapati., J. K. Johnson, and D. S. Sholl. "Predicting Reaction Equilibria for Destabilized Metal Hydride Decomposition Reactions for Reversible Hydrogen Storage,". *The Journal of Physical Chemistry C*, 111(4):1584–1591, **2007**.

[37] D. J. Siegel, C. Wolverton, and V. Ozoliņš. "Thermodynamic guidelines for the prediction of hydrogen storage reactions and their application to destabilized hydride mixtures,". *Phys. Rev. B*, 76:134102, Oct **2007**.

[38] C. Wolverton, D. J Siegel, A. R. Akbarzadeh, and V. Ozoliņš. "Discovery of novel hydrogen storage materials: an atomic scale computational approach,". *Journal of Physics: Condensed Matter*, 20(6):064228, **2008**.

[39] Ki Chul Kim and D. S. Sholl. "Crystal Structures and Thermodynamic Investigations of LiK(BH4)2, KBH4, and NaBH4 from First-Principles Calculations,". *The Journal of Physical Chemistry C*, 114(1):678–686, **2010**.

[40] J. Yang, A. Sudik, D. J. Siegel, D. Halliday, A. Drews, R. O Carter, C. Wolverton, G. J. Lewis, J. W. Sachtler, J. J. Low, S.A. Faheem, D. A. Lesch, and V. Ozolins. "A Self-Catalyzing Hydrogen-Storage Material,". *Angew. Chem. Int. Ed. Engl*, 47:882–887, **2008**.

[41] P. Atkins and R. Friedman. *Molecular Quantum Mechanics*. Oxford University Press, **2005**.

[42] K. Burke. *The abc of DFT*, **2007**.

[43] K. Capelle. *A bird's-eye view of density-functional theory*. Departamento de Física e Informática, Instituto de Física de São Carlos-USP, **2004**.

[44] R. Parr and W. Yang. *Density-functional theory of atoms and molecules. International series of monographs on chemistry*. Oxford University Press, **1994**.

[45] D. Sholl and J. Steckel. *Density functional theory: a practical introduction*. Wiley, **2009**.

[46] W. Koch and M. HoltHausen. *A chemist's guide to density functional theory*. WILEY-VCH Verlag, **2000**.

[47] P. Hohenberg and W. Kohn. Inhomogeneous electron gas. *Phys. Rev.*, 136:B864–B871, Nov **1964**.

[48] W. Kohn and L. J. Sham. Self-consistent equations including exchange and correlation effects. *Phys. Rev.*, 140:A1133–A1138, Nov **1965**.

[49] M. Levy. "Electron densities in search of Hamiltonians,". *Phys. Rev. A*, 26:1200–1208, Sep **1982**.

[50] N. Argaman and G. Makov. "Density functional theory: An introduction,". *Am J Phys*, 68:69–79, **2000**.

[51] S. F. Sousa, P. A. Fernandes, and M. J. Ramos. "General Performance of Density Functionals,". *The Journal of Physical Chemistry A*, 111(42):10439–10452, **2007**.

[52] G. Kresse and J. Hafner. "Ab initio molecular dynamics for liquid metals,". *Phys. Rev. B*, 47:558–561, Jan **1993**.

[53] G. Kresse and J. Furthmüller. "Efficient iterative schemes for *ab initio* total-energy calculations using a plane-wave basis set,". *Phys. Rev. B*, 54:11169–11186, Oct **1996**.

[54] K. Burke and L. O. Wagner. "DFT in a Nutshell,". *International Journal of Quantum Chemistry*, 113:96–101, **2013**.

[55] J. Tao, J. P. Perdew, V. N. Staroverov, and G. E. Scuseria. "Climbing the Density Functional Ladder: Nonempirical Meta-Generalized Gradient Approximation Designed for Molecules and Solids,". *Phys. Rev. Lett.*, 91(14):146401, Sep **2003**.

[56] V. N. Staroverov, G. E. Scuseria, J. Tao, and J. P. Perdew. "Comparative assessment of a new nonempirical density functional: Molecules and hydrogen-bonded complexes,". *The Journal of Chemical Physics*, 119(23):12129–12137, **2003**.

[57] J. P. Perdew, J. Tao, V. N. Staroverov, and G. E. Scuseria. "Meta-generalized gradient approximation: Explanation of a realistic nonempirical density functional,". *The Journal of Chemical Physics*, 120(15):6898–6911, **2004**.

[58] V. N. Staroverov, G. E. Scuseria, J. Tao, and J. P. Perdew. "Tests of a ladder of density functionals for bulk solids and surfaces,". *Phys. Rev. B*, 69(7):075102, **2004**.

[59] D. R. Hamann, M. Schlüter, and C. Chiang. "Norm-Conserving Pseudopotentials. *Physical Review Letters*, 43(20):1494–1497, November **1979**.

[60] L. Kleinman and D. M. Bylander. "Efficacious Form for Model pseudopotentials,". *Phys. Rev.Lett*, 48(20):1425–1428, **1982**.

[61] D.R. Hamann. "Generalized norm-conserving pseudopotentials,". *Phys. Rev. B*, 40:2980–2987, August **1989**.

[62] E. L. Shirley, D. C. Allan, R. M. Martin, and J. D. Joannopoulos. "Extended norm-conserving pseudopotentials,". *Phys. Rev. B*, 40(6):3652–3660, August **1989**.

[63] D. Vanderbilt. "Soft self-consistent pseudopotentials in a generalized eigenvalue formalism,". *Physical Review B*, 41(11):7892–7895, April **1990**.

[64] N. Troullier and J. L. Martins. "Efficient pseudopotentials for plane-wave calculations,". *Phys. Rev. B*, 43(3):1993–2006, January **1991**.

[65] D.M. Bylander I. Morrison and L.Kleinman. "Nonlocal hermitian norm-conserving vanderbilt pseudopotential,". *Phys. Rev. B*, 47(6728-6731), **1993**.

[66] D.R. Hamman G.B. Bachelet and M.Schlüter. "Pseudopotentials that work: From h to pu,". *Phys. Rev. B*, 26(8):4199–4228, **1982**.

[67] P.E. Blöchl. "Generalized separable potentials for electronic-structure calculations,". *Phys. Rev. B*, 41(8):5414–5416, **1990**.

[68] R.P. Feynman. Forces in molecules. *Phys. Rev.*, 56(4):340–344, **1939**.

[69] R. Car and M. Parrinello. "Unified approach for molecular dynamics and density-functional theory,". *Physical Review Letters*, 55(22):2471–2474, November **1985**.

[70] H. C. Andersen. "Molecular dynamics simulations at constant pressure and/or temperature,". *J.Chem.Phys*, 72(4):2384–2393, February **1980**.

[71] N. Ashcroft and N. Mermin. *Solid state physics. Holt-Saunders International Editions*, **1976**.

[72] J. Blakemore. *Solid State Physics. Cambridge University Press*, **1985**.

[73] C.Elsässer W. Frank and M. Fähnle. "Ab initio force-constant method for phonon dispersions in alkali metals,". *Phys. Rev.Lett*, 74(10):1791–1794, **1995**.

[74] K.Parlinski, Z. Q. Li, and Y. Kawazoe. "First-principles determination of the soft mode in cubic ZrO_2,". *Phys. Rev.Lett*, 78(21):4063–4066, **1997**.

[75] C. Kittel. *Introduction to solid state physics.* Wiley, **2005**.

[76] H. Ibach and H. Lüth. *Solid-State Physics,.* Springer-Verlag, **2003**.

[77] V.Ozolins C.Wolverton and M. Asta. "Hydrogen in aluminum: First-principles calculations of structure and thermodynamics,". *Phys. Rev. B*, 69(14):144109, **2004**.

[78] C.Kittel and H. Kroemer. *Thermal Physics*. W.H. Freeman, **1980**.

[79] P. Atkins and J.Paula. *Physical Chemistry*. W.H. Freeman, **2002**.

[80] P. Chen, Z. Xiong, J. Luo, J. Lin, and K. L. Tan. "Interaction of hydrogen with metal nitrides and imides,". *Nature*, 420(6913):302–304, **2002**.

[81] D.A. Ponomarev and V.V. Takhistov. "Thermochemistry of organic and elementoorganic species. Part III. The enthalpies of formation of the hydrides of main group elements,". *Journal of Molecular Structure*, 477(1–3):91 – 103, **1999**.

[82] Ewald Veleckis. "Decomposition pressures in the (+) fields of the Li-LiH, Li-LiD, and Li-LiT systems,". *Journal of Nuclear Materials*, 79(1):20 – 27, **1979**.

[83] H. Cao, Y. Zhang, J. Wang, Z. Xiong, G. Wu, and P. Chen. "Materials design and modification on amide-based composites for hydrogen storage,". *Progress in Natural Science: Materials International*, 22(6):550 – 560, **2012**.

[84] W. Grochala and P. P. Edwards. "Thermal Decomposition of the Non-Interstitial Hydrides for the Storage and Production of Hydrogen,". *Chem. Rev*, 104(3):1283–1316, **2004**.

[85] A.T.W. Kempen, F. Sommer, and E.J. Mittemeijer. 'Determination and interpretation of isothermal and non-isothermal transformation kinetics; the effective activation energies in terms of nucleation and growth,". *Journal of Materials Science*, 37(7):1321–1332, **2002**.

[86] F.E. Pinkerton. "Decomposition kinetics of lithium amide for hydrogen storage materials,". *Journal of Alloys and Compounds*, 400(1–2):76 – 82, **2005**.

[87] T. Markmaitree, T. Ren, and L. L. Shaw. "Enhancement of Lithium Amide to Lithium Imide Transition via Mechanical Activation,". *The Journal of Physical Chemistry B*, 110(41):20710–20718, **2006**.

[88] W. I. F. David, M. O. Jones, D. H. Gregory, C. M. Jewell, S. R. Johnson, A. Walton, and P. P. Edwards. "A Mechanism for Non-stoichiometry in the Lithium Amide/Lithium Imide Hydrogen Storage Reaction,". *Journal of the American Chemical Society*, 129(6):1594–1601, **2007**.

[89] P. Chen, X. Zhitao, J. Lin, and L. T. Kuang. "Interaction between Lithium Amide and Lithium Hydride,". *J.Phys.Chem. B*, 107:10967–10970, **2003**.

[90] K. Hoang, A. Janotti, and C. G. Van de Walle. "Mechanisms for the decomposition and dehydrogenation of Li amide/imide,". *Phys. Rev. B*, 85(6):064115, Feb **2012**.

[91] H. Gunaydin, K. N. Houk, and V. Ozoliņš. "Vacancy-mediated dehydrogenation of sodium alanate,". *Proceedings of the National Academy of Sciences*, 105(10):3673–3677, **2008**.

[92] K. J. Michel and V. Ozoliņš. "Site substitution of Ti in $NaAlH_4$ and Na_3AlH_6,". *The Journal of Physical Chemistry C*, 115(43):21454–21464, **2011**.

[93] K. J. Michel and V. Ozoliņš. "Vacancy diffusion in $NaAlH_4$ and Na_3AlH_6,". *The Journal of Physical Chemistry C*, 115(43):21465–21472, **2011**.

[94] K. J. Michel and V. Ozolins. "Theory of mass transport in sodium alanate,". *J. Mater. Chem. A*, 2(12):4438–4448, **2014**.

[95] A. Peles and C. G. Van de Walle. "Role of charged defects and impurities in kinetics of hydrogen storage materials: A first-principles study,". *Phys. Rev. B*, 76:214101, Dec **2007**.

[96] J. Perdew and Y. Wang. "Accurate and simple analytic representation of the electron-gas correlation energy,". *Phys. Rev. B*, 45(23):13244 – 13249, **1992**.

[97] T. Tsumuraya, T. Shishidou, and T. Oguchi. "First-principles study on lithium and magnesium nitrogen hydrides for hydrogen storage,". *Journal of Alloys and Compounds*, 446–447(0):323 – 327, **2007**.

[98] V. H. Jacobs and R. Z. Juza. "Neubestimmung der Kristallstruktur des Lithiumamids,". *Anorg Allg Chem*, 391:271–279, **1972**.

[99] T. Mueller and G. Ceder. "Effective interactions between the N-H bond orientations in lithium imide and a proposed ground-state structure,". *Phys. Rev. B*, 74:134104, Oct **2006**.

[100] K. J. Jay Michel and V. Ozoliņš. "Native Defect Concentrations in NaAlH4 and Na3AlH6,". *The Journal of Physical Chemistry C*, 115(43):21443–21453, **2011**.

[101] C. G. Van de Walle and J. Neugebauer. "First-principles calculations for defects and impurities: applications to III-nitrides,". *Journal of Applied Physics.*, 95(8):3851–3879., **2004**.

[102] H. Jonsson, G. Mills, and K. W. Jacobsen. *Classical and Quantum Dynamics in Condensed Phase Simulations*. World Scientific, **1998**.

[103] H. Bracht. "Diffusion Mechanisms and Intrinsic Point-Defect Properties in Silicon,". *MRS Bulletin*, 25(6):22–27, 6 **2000**.

[104] J.W Wiench, V.P Balema, V.K Pecharsky, and M Pruski. "Solid-state 27Al {NMR} investigation of thermal decomposition of LiAlH4,". *Journal of Solid State Chemistry*, 177(3):648 – 653, **2004**.

[105] A. Andreasen. "Effect of Ti-doping on the dehydrogenation kinetic parameters of lithium aluminum hydride,". *Journal of Alloys and Compounds*, 419:40–44, **2006**.

[106] Z. Li, P. Li, Q. Wan, F. Zhai, Z. Liu, K. Zhao, L. Wang, S. Lü, L. Zou, X. Qu, and A. A. Volinsky. "Dehydrogenation Improvement of LiAlH4 Catalyzed by Fe2O3 and Co2O3 Nanoparticles,". *The Journal of Physical Chemistry C*, 117(36):18343–18352, **2013**.

[107] A. Andreasen, T. Vegge, and A. S. Pedersen. "Dehydrogenation kinetics of as-received and ball-milled,". *Journal of Solid State Chemistry*, 178(12):3672 – 3678, **2005**.

[108] T. Sun, C.K. Huang, H. Wang, L.X. Sun, and M. Zhu. "The effect of doping NiCl2 on the dehydrogenation properties of LiAlH4,". *International Journal of Hydrogen Energy*, 33(21):6216 – 6221, **2008**.

[109] J. Chen, N. Kuriyama, Q. Xu, H. T. Takeshita, and T. Sakai. "Reversible Hydrogen Storage via Titanium-Catalyzed LiAlH4 and Li3AlH6,". *The Journal of Physical Chemistry B*, 105(45):11214–11220, **2001**.

[110] X. Liu, G. S. McGrady, H. W. Langmi, and C. M. Jensen. "Facile Cycling of Ti-Doped LiAlH4 for High Performance Hydrogen Storage,". *Journal of the American Chemical Society*, 131(14):5032–5033, **2009**. PMID: 19296609.

[111] F. Zhai, P. Li, A. Sun, S. Wu, Q. Wan, W. Zhang, Y. Li, L. Cui, and X. Qu. "Significantly Improved Dehydrogenation of LiAlH4 Destabilized by MnFe2O4 Nanoparticles,". *The Journal of Physical Chemistry C*, 116(22):11939–11945, **2012**.

[112] D. Blanchard, H.W. Brinks, B.C. Hauback, P. Norby, and J. Muller. "Isothermal decomposition of LiAlD4 with and without additives,". *Journal of Alloys and Compounds*, 404–406(0):743 – 747, **2005**.

[113] K. Hoang, A. Janotti, and C. G. Van de Walle. "Decomposition mechanism and the effects of metal additives on the kinetics of lithium alanate,". *Phys. Chem. Chem. Phys.*, 14:2840–2848, **2012**.

[114] A.S. Nowick and G.G. Libowitz, editors. *Diffusion in Crystalline solids*. Academic Press, Inc., **1984**.

[115] U. Gösele, F. Morehead, W. Frank, and A. Seeger. "Diffusion of gold in silicon: A new model,". *Applied Physics Letters*, 38(3):157–159, **1981**.

[116] U. Gösele, W. Frank, and A. Seeger. "The influence of intrinsic defects on the degradation and luminescence of GaAs and other III-V compounds,". *Appl. Phys.*, 23(3):303–309, **1980**.

[117] H. Mehrer. "Atomic jump processes in self-diffusion,". *Journal of Nuclear Materials*, 69–70(0):38 – 60, **1978**.

[118] N.L. Peterson. "Self-diffusion in pure metals,". *Journal of Nuclear Materials*, 69–70(0):3 – 37, **1978**.

[119] A.D. Le Claire. "Solute diffusion in dilute alloys,". *Journal of Nuclear Materials*, 69–70(0):70 – 96, **1978**.

[120] M. Y. L. Jung, R. Gunawan, R. D. Braatz, and E. G. Seebauer. "Pair Diffusion and Kick-out: Contributions to Diffusion of Boron in Silicon,". *American Institute of Chemical Engineers*, 50(12), **2004**.